

## A METHOD BASED ON WAVELET TRANSFORMS FOR SOURCE DETECTION IN PHOTON-COUNTING DETECTOR IMAGES. II. APPLICATION TO ROSAT PSPC IMAGES

F. DAMIANI, A. MAGGIO, G. MICELA, AND S. SCIORTINO

Istituto ed Osservatorio Astronomico di Palermo “G. S. Vaiana,” Piazza del Parlamento 1, 90134 Palermo, Italy;  
damiani@oapa.astropa.unipa.it, maggio@oapa.astropa.unipa.it, gmicela@oapa.astropa.unipa.it,  
sciorti@oapa.astropa.unipa.it

Received 1996 July 26; accepted 1997 January 28

### ABSTRACT

We apply to the specific case of images taken with the *ROSAT* PSPC detector our wavelet-based X-ray source detection algorithm presented in a companion paper. Such images are characterized by the presence of detector “ribs,” strongly varying point-spread function, and vignetting, so that their analysis provides a challenge for any detection algorithm. First, we apply the algorithm to simulated images of a flat background, as seen with the PSPC, in order to calibrate the number of spurious detections as a function of significance threshold and to ascertain that the spatial distribution of spurious detections is uniform, i.e., unaffected by the ribs; this goal was achieved using the exposure map in the detection procedure. Then, we analyze simulations of PSPC images with a realistic number of point sources; the results are used to determine the efficiency of source detection and the accuracy of output quantities such as source count rate, size, and position, upon a comparison with input source data. It turns out that sources with 10 photons or less may be confidently detected near the image center in medium-length ( $\sim 10^4$  s), background-limited PSPC exposures. The positions of sources detected near the image center (off-axis angles  $< 15'$ ) are accurate to within a few arcseconds. Output count rates and sizes are in agreement with the input quantities, within a factor of 2 in 90% of the cases. The errors on position, count rate, and size increase with off-axis angle and for detections of lower significance. We have also checked that the upper limits computed with our method are consistent with the count rates of undetected input sources. Finally, we have tested the algorithm by applying it on various actual PSPC images, among the most challenging for automated detection procedures (crowded fields, extended sources, and nonuniform diffuse emission). The performance of our method in these images is satisfactory and outperforms those of other current X-ray detection techniques, such as those employed to produce the MPE and WGA catalogs of PSPC sources, in terms of both detection reliability and efficiency. We have also investigated the theoretical limit for point-source detection, with the result that even sources with only 2–3 photons may be reliably detected using an efficient method in images with sufficiently high resolution and low background.

*Subject headings:* methods: data analysis — methods: statistical — techniques: image processing —  
X-rays: stars

### 1. INTRODUCTION

In a companion paper (Damiani et al. 1997, hereafter Paper I) we have presented the general properties of a source detection method based on wavelet transforms (WT), purposely developed to work on X-ray astronomical images. Our method tries to obviate difficulties encountered using other methods, based, e.g., on sliding window or maximum likelihood techniques, and implemented within various astronomical software packages. Such difficulties include the lack of sensitivity in image regions where spatial resolution is severely degraded, the failure to take best advantage of the detector spatial resolution to separate close sources, and the occurrence of (many) spurious detections in the wings of extended sources, or in the presence of diffuse emission.

To summarize, our method is based on the property of wavelet transforms of providing a multiscale analysis of the data, which allows us to study structures (detect sources) with a large range of sizes. This is useful not only for detecting actually extended sources, but also and more commonly for detecting point sources smeared by the detector point-spread function (PSF), whose size may vary widely across the image. Our implementation of the algorithm makes use

of the exposure map of each observation needed to treat properly exposure variations across the image. A detailed study of the statistical properties of the wavelet-transformed background noise enables us to discriminate efficiently sources from background fluctuations, to any desired confidence level. As explained in Paper I, we speak of “confidence level” and not of “signal-to-noise ratio” to indicate the probability that a given detection is not a background fluctuation. For convenience, we will often express such a probability in terms of Gaussian  $\sigma$  values (for example, a confidence level of  $3\sigma$  corresponds to a probability  $P = 1 - 0.9973$  that a source is a spurious background fluctuation); this, however, does not imply that the signal-to-noise ratio of a  $3\sigma$  source has a value of 3, since determining the probability of the existence of a source is a different problem from measuring its flux (and error). After having completed source detection proper, the count rate and size are determined for each source, using WT as well. Briefly, sources are selected as spatial maxima of the WT, with amplitude significant enough compared to the local background; the amplitude of the WT maximum associated with a source is, however, a function of the WT scale  $a$ ,  $w(a)$ , whose shape yields information on source intensity and size

(see Paper I for details). The same method allows us also to estimate consistently upper limits on the count rate of undetected objects in the field of view.

In this paper, we apply our detection algorithm to the case of X-ray images taken with the PSPC detector (Pfeffermann et al. 1986) on board the *ROSAT* satellite. Since PSPC images have a complex structure, each of the techniques developed in Paper I finds application in their analysis. We describe in § 2 how the method needs to be specialized in order to be applied to PSPC images. Then, in § 3 we present tests of our method's performances, on both simulated and real PSPC data; the use of simulated images permits to study the efficiency and reliability of the method under controlled conditions. In connection with the results obtained, § 4 is a discussion of the theoretical limit for point-source detection. Finally, § 5 is a summary of the results obtained, and a discussion of the applicability of our detection method to X-ray images obtained using other X-ray detectors.

## 2. APPLICATION TO PSPC IMAGES

The *ROSAT* PSPC has a field of view of about  $1^\circ$  radius, and coupled with the *ROSAT* X-ray telescope is sensitive to X-rays in the energy range 0.1–2.0 keV. The PSF width is  $\sigma_{\text{PSF}} \sim 18''$  on-axis and widens to 1'.0 for off-axis angles of  $30'$ , and 2'.7 for off-axis angles of  $60'$ . Typically, the background intensity in PSPC images is  $1.5 \times 10^{-3}$  counts arcmin $^{-2}$  s $^{-1}$  (including all components). During the years 1990–1993, the great majority of all known X-ray sources has been imaged with this detector (more than 50,000 sources, from both the *ROSAT* All-Sky Survey and pointed observations). PSPC images are characterized by properties that are strong functions of position within the field of view. The PSF distorts and strongly increases in size with off-axis angle ( $\theta > 20'$ ), because the Wolter optics of the X-ray telescope do not correct for coma or higher order distortions (Gursky & Schwartz 1974) and so do not produce sharply focused images off-axis. The effective exposure is also a function of position, since there is a reduction of telescope effective area away from the optical axis (vignetting), and especially since the detector window support structures (ribs) produce deep shadows on the focal plane. However, since the satellite pointing during normal operation is not fixed but oscillates around the nominal position (wobbling), the obscuration produced by ribs is smeared. Therefore, the rib shadow is not completely dark, and bright X-ray sources may be detected even below ribs. As explained in Paper I, our detection algorithm takes into account exposure variations across the image, which are described by the exposure map associated with each observation (Snowden et al. 1994), yielding the total effective exposure at each location in the image.

We find it convenient to apply our algorithm to images rebinned with a pixel size of  $15''$  (the full pixelation being  $0'.5$ ). This allows us both a fair sampling of the PSF at image center ( $\sigma_{\text{PSF}} = 18''$  at an energy  $E = 0.3$  keV), and to keep the whole image within tractable dimensions ( $512 \times 512$  pixels). The scales at which we compute the WT range from 1 to 16 image pixels ( $15''$  to  $4'$ ), in steps of a factor  $2^{1/2}$ . This choice allows us to cover the broad range of variation of the PSF size across the image ( $\sigma_{\text{PSF}} = 2'.7$  at image edge for  $E = 0.3$  keV) and also to detect moderately extended sources.

The spatial grid on which the WT is computed has a

spacing of 1 pixel ( $15''$ ) at the smallest scales  $a$ , and wider at higher scales; however, when the “best” position for a given detection is searched, the WT grid spacing is lowered to 0.5 pixels ( $7'.5$ ) in the central region of the image (off-axis angle less than  $30'$ ), so that the nominal positional accuracy of detected source positions is as low as 0.25 pixels, or  $3'.75$ , near the image center. A grid spacing of 1 pixel is instead adopted outside this central region, where the PSF is much broadened, doubling the nominal position error.

While the detection itself of a source with our algorithm does not require a detailed knowledge of the detector PSF, the determination of its count rate and size may only be made if the PSF shape is known (and this holds true for the computation of upper limits as well). In Paper I (see §§ 2 and 4), we assumed that the PSF at a given location in the image has a simple Gaussian shape, but this is not accurate for typical X-ray detectors and for the PSPC in particular (Hasinger et al. 1993a). Here we study to what extent the assumed Gaussian approximation of the actual PSF can be considered satisfactory. Since we are working entirely using WT images, and the information on source properties is derived from the measured profile of the function  $w(a)$  (Paper I, §§ 2 and 4.5), we test if such a function  $w(a)$  computed using the actual PSPC PSF is significantly different from the function  $w(a)$  computed assuming a Gaussian PSF. The azimuthally averaged PSF of the PSPC has been studied by Hasinger et al. (1993a), and adopting their parametrization we have computed the new function  $w(a)$ , as described in detail in Appendix A: it turns out that the Gaussian approximation for the PSF is good (see Fig. 15 below), especially for scales  $a \sim a_{\text{max}}$  where the function  $y(a) = w(a)/a$  has its maximum, which is used to derive the source count rate and size. Errors in the derived count rates due to the adoption of a Gaussian PSF are at most 9% (especially for very hard sources on-axis) but are negligible ( $\leq 1\%$ ) in most cases. Errors on the derived sizes are even smaller, being about 3% at most.

## 3. TESTING AND CALIBRATION OF THE ALGORITHM

### 3.1. Application to Simulated PSPC Background Images

In order to test the overall performance of our detection algorithm, it is of primary importance to be sure that it does not yield a large number of spurious sources in the final output, e.g., because of unrejected background fluctuations or detector peculiarities not properly handled (e.g., ribs and edges). For a given detector, the number of spurious detections is a function of the detection threshold we choose, namely, the significance level  $k\sigma$ , which we will determine in this section with the help of numerical simulations.

Our purpose here is to determine how many spurious detections are found by the algorithm in the case of pure background emission, as imaged with the PSPC. The simulated image data must therefore include shadows due to ribs and the effect of wobbling on the whole image. To this aim, we started from exposure maps computed for real PSPC observations, including cases with normal, reduced, and zero wobbling amplitude, respectively. Assuming a total (vignetted plus particle) PSPC background rate of  $1.5 \times 10^{-3}$  counts arcmin $^{-2}$  s $^{-1}$  at image center (e.g., Bocchino, Maggio, & Sciortino 1994), we have computed the background density near image center for exposure times in the range between 500–50,000 s; then, this background density is scaled in all parts of the image according

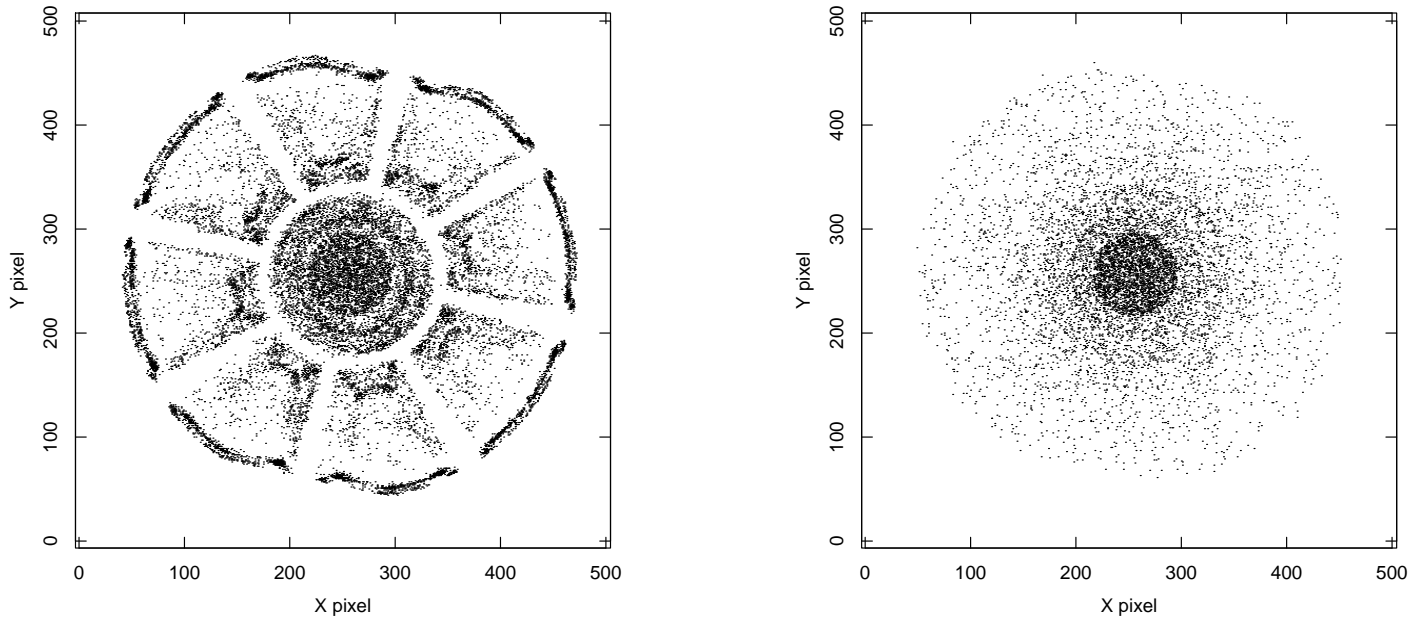


FIG. 1.—Spatial distribution of spurious sources: (a) the WT is computed on the photon image; the excess of spurious detections along the ribs and the image edge is evident. (b) The WT is computed on the count rate image; note that no excess of spurious detections is present in this case. The higher density of spurious detections in concentric circular regions toward the image center is expected and is due to the larger number of “trials” made by the algorithm in the inner part of the image, since it contains more resolution elements and is analyzed at more scales  $a$  than the outer regions.

to the exposure map, and the (integer) number of counts in each image pixel is eventually computed by randomizing the resulting value according to the proper Poisson distribution, pixel by pixel. This yields the appropriate photon statistics in each pixel of the simulated image.

We have performed 200 realizations of such simulated background images for each exposure map and exposure time and then applied to them the detection code and recorded the properties of all (spurious) detections. In Figure 1 we show the spatial distribution of all sources detected in 200 simulations above a significance level of  $3\sigma$  (for an exposure map derived from the PSPC observation RP200068, scaled to an exposure time of 10,000 s): Figure 1a pertains to an earlier version of the algorithm, which worked on the *photon* (not count rate) image, and without edge correction, while Figure 1b is the output of the final version of the algorithm, which works on the *count rate* image (see Paper I). It is obvious that ribs and edges cause ripples in the WT of the background, which are often interpreted as sources and must be corrected for, as we do in the final version, which produces a uniform spatial distribution of spurious detections. The appearance of concentric circles of increasing source density toward the image center in Figure 1b is due to the larger number of “trials” made by the algorithm in this region, since it contains more resolution elements and is analyzed at more scales  $a$  than the outer regions (detection at each scale  $a$  is done only within an assigned maximum off-axis angle such that  $\sigma_{\text{PSF}} \leq a$ ; see Paper I). We have verified that the spatial distribution of detections at each scale is indeed uniform over the analyzed region, even in the radial direction (these distributions are shown in Fig. 2 for scales  $a = 0.5'$  and  $a = 2'$ , respectively). These simulations are not needed simply to set appropriate values for the method’s free parameters, such as the threshold significance level  $k\sigma$ , but

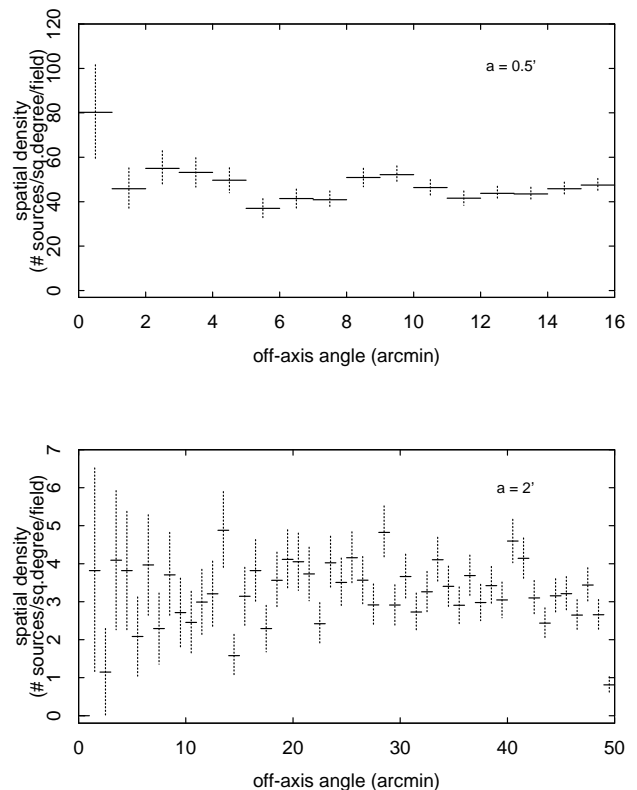


FIG. 2.—Radial distribution of spurious detections (averaged over annuli), for scales  $a = 0.5'$  (top) and  $a = 2'$  (bottom). The error bars are Poisson errors on the total number of detections in each off-axis bin. Both cases are compatible with a uniform distribution. In particular, note that there is no excess of spurious detections at either the position of the circular rib (off-axis  $\sim 22'$ ) or along the image edge ( $\sim 50'$ ).

they have provided a continuous feedback in the development of our algorithm.

We show in Figure 3 the cumulative number of spurious detections (per field) as a function of their significance, regardless of position, for the final version (using the same exposure map as in Fig. 1b). The lower curves show the distribution of spurious detections at each scale separately, before cross-identification between different scales (Paper I, § 4.3); these distributions have nearly similar slopes for all detection scales. The upper solid curve (*thick line*) shows instead the distribution of the final, cross-identified sources, regardless of detection scale; we see that in order to have one spurious detection per field (in a random position), we need to use a significance threshold of  $4.35 \sigma$ . For significance levels in the range  $3.5\text{--}5.0 \sigma$ , the cumulative number of spurious detections is found to follow approximately the law:  $\log N_{\text{spurious}}(>k\sigma) = 5.82 - 1.34k$  (Fig. 3, *thin solid line*). We have verified that the significance threshold to be used in order to have an assigned number of spurious detections per field varies little as a function of both background density and exposure map chosen.

### 3.2. Application to Simulated PSPC Images with Sources

No less important than establishing the expected number of spurious sources per field is knowing the efficiency for detecting real, weak sources. We have studied this through the analysis of simulated PSPC images, containing point sources superposed on the background. The comparison between the position, intensity, and size of the input simulated sources and the corresponding output quantities of the algorithm for the same sources allows us to evaluate empirically the errors on such quantities.

The simulated PSPC images must be as realistic as possible to allow a detailed test of the algorithm. We have followed the same method of simulation of the previous subsection but have added the contribution of sources to the “noiseless” image before randomizing it. The source positions are generated randomly with a uniform distribution across the field of view. The spatial distribution of photons for each source (i.e., the source PSF, dependent on off-axis angle and energy) has been modeled in full detail, following the parameterization given by Hasinger et al. (1993a), assuming for the simulated sources a monoenergetic PSF with energy  $E = 0.3 \text{ keV}$ .<sup>1</sup> The intensity distribution of the simulated sources has been taken to be equal to the  $\log N\text{--}\log S$  relation presented by Hasinger et al. (1993b). These simulations consist of 50 realizations each, for different combinations of exposure times and background values, to test the algorithm performances under a variety of conditions. One such simulated image is shown in Figure 4, containing 977 simulated sources down to a minimum of 5 photons, for an exposure time of 10 ks, corresponding to a minimum source flux  $f_x = 2.8 \times 10^{-15} \text{ ergs s}^{-1} \text{ cm}^{-2}$ . We have purposely included in the simulated images many sources below the detection threshold, to test the algorithm performances in a situation as realistic as possible.

<sup>1</sup> This value has been chosen such that the monoenergetic PSF shape best approximates the shape of a spectrum-weighted PSF (namely, the radius of the circle containing 90% of the source photons is within about 10% of the actual spectrum-weighted value in the broadband) over the whole field of view, for both thermal models with  $\log T = 6.5\text{--}7.0 \text{ K}$  and power-law spectra with an index in the range  $0.5\text{--}1.5$  and with absorption up to  $N_{\text{H}} = 10^{21} \text{ cm}^{-2}$ .

Applying the detection algorithm to these simulated images, we obtain lists of detected sources, to be compared with the input (simulated) source lists. This allows us to determine the efficiency of source detection, as a function of source counts, and off-axis angle. We cross-identify each detected source with input counterparts by positional matching within  $1.5 \times \max(\sigma_{\text{PSF}}, a_{\text{max}})$  (Paper I). The detections with one single input counterpart, found especially in the center of field of view, allow the most accurate comparison between input and detected source properties. In the case of detections matching the position of multiple input counterparts, the input counts of all these counterparts were summed to perform a meaningful comparison with the counts of the detected source, since only their cumulative signal is relevant for detection, while individual contributions are disregarded in the following.<sup>2</sup> A few detections, moreover, have no plausible counterpart, allowing us to assess the number of spurious detections in the presence of other sources. It turns out that the number of spurious detections is the same, within uncertainties, as in the case of pure background images (§ 3.1).

Figure 5 shows the detection efficiency versus (cumulative) source counts, for various ranges of off-axis angles, i.e., the fraction of detections  $N_{\text{det}}/(N_{\text{det}} + N_{\text{undet}})$ . Here and in the following plots the detection threshold is set to  $4.2 \sigma$ , yielding about 1.8 spurious sources per field. The number of counts required for a source to be detected with a probability of 50% is about  $N_{\text{src}} = 20$  at field center, and it increases monotonically toward the outer regions. This is *not* due to vignetting, which affects the conversion between raw counts and rates, while we are here dealing with raw imaged counts. The reason is instead the strong increase of  $\sigma_{\text{PSF}}$  outward and the corresponding strong increase of background noise in the source region. The curves shown are derived using a simulated image background of 15 counts  $\text{arcmin}^{-2}$ ; they shift leftward for a lower background, giving less noise in the source region, and rightward for a higher background. We have tested the low-background case with an additional set of simulations, with the same number of sources per field and same exposure time, but with a background 10 times lower (1.5 counts  $\text{arcmin}^{-2}$ ); as expected, the curves of Figure 5 shift toward lower source counts. At image center, sources having as little as 11 counts can be detected with efficiency of 50%, and sources with only 7 counts, with 10% efficiency.

We have also performed comparisons between cumulative input source counts and those estimated for detections by the algorithm (Fig. 6). These were estimated in two ways, as explained in Paper I (§ 4.5): small dots are low-significance detections, whose counts are estimated simply from the values of WT at the maximum significance scale  $a_{\text{max}}$ , while crosses indicate higher significance detections, whose counts are derived from two points of the profile  $y(a)$  versus  $a$ . As is plausible, there is a larger scatter for sources with a low number of counts ( $<100$ ), the relationship becoming tighter for more intense sources; the vast major-

<sup>2</sup> To be more precise, we not only need to sum all counts from input candidate counterparts to a given detection, lying where the generating wavelet has its peak, but we must also subtract counts of other sources falling in the negative annulus of the generating wavelet, and therefore contributing to the local background, since the wavelet transform indeed measures the signal excess relative to neighboring locations, not just the total signal in a region.

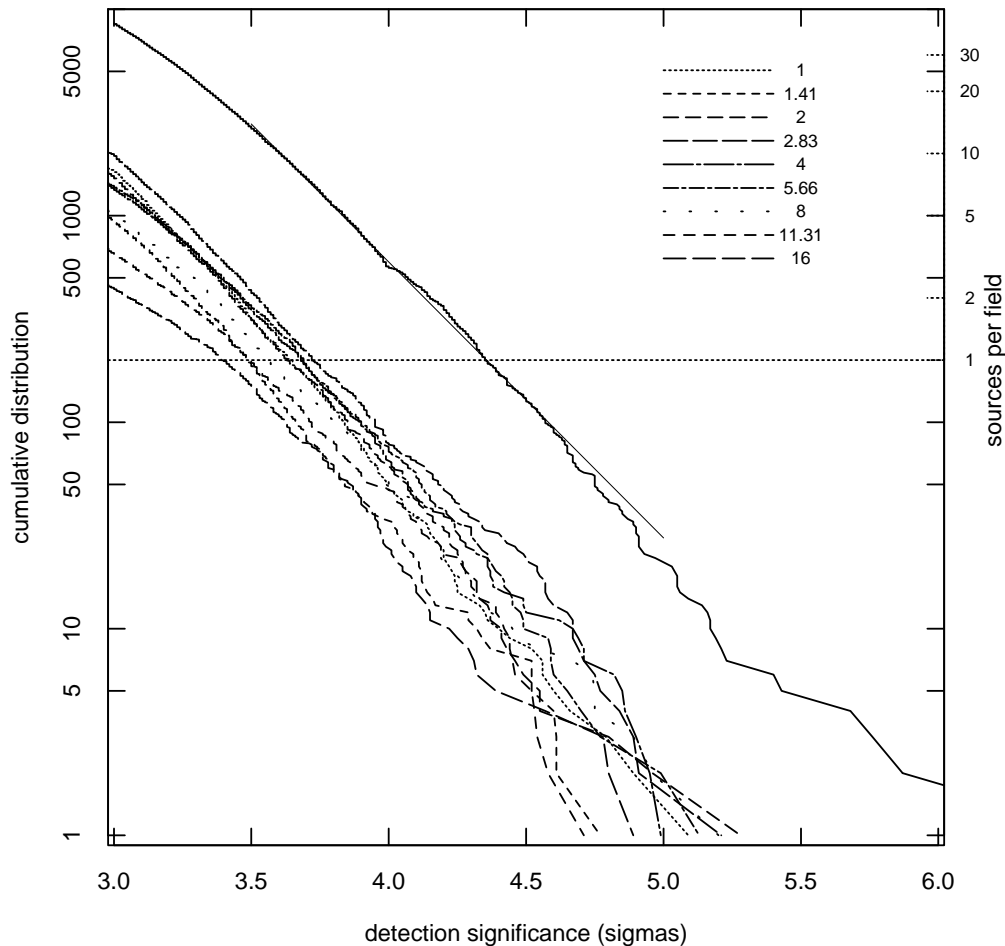


FIG. 3.—Cumulative number of spurious detections vs. significance level  $k\sigma$ . These distributions are derived from a set of 200 simulations of pure background PSPC fields with exposure time of 10 ks and a typical PSPC background of  $1.5 \times 10^{-3}$  counts  $s^{-1}$  arcmin $^{-2}$  (using the exposure map of the image RP200068). The top thick solid line refers to the final source list (after cross-identification of detections at different scales  $a$ ), while the lower distributions refer to detections at various scales separately, as indicated. Also indicated with a thin solid line is the linear fit to the overall distribution for detections in the significance range 3.5–5.0  $\sigma$ . The scale on the right-hand side (dotted tick marks on  $y$ -axis) indicates the number of spurious detections per image. The horizontal dotted line indicates the level of one spurious detection per simulated field.

ity of detected sources have estimated counts within a factor of 2 from the input values. More quantitative statements are difficult to make, since, as Figure 6 shows, the relation between detected and input counts is asymmetrical at low counts: sources with few input counts (prior to randomization) are preferentially detected if they come out as positive random fluctuations, and they remain undetected if they come out as negative fluctuations. The relation is slightly tighter for detections with a single counterpart and for sources in the central part of the field of view (not shown in the figure).

We have also tested the accuracy of errors on source counts, derived as explained in Paper I. Figure 7 shows a histogram of the difference between input and detected source counts, divided by the computed error. If errors are correctly computed, the distribution of such a quantity should be close to a Gaussian, with zero mean and unit variance. Such a Gaussian shape is also shown in Figure 7, and we can see that its width indeed matches the histogram variance quite well; the histogram mean is instead lower than zero, mostly because of very weak input sources, whose count rate is overestimated by the WT algorithm, as explained above.

Figure 8 shows a comparison between detected and input source (apparent) sizes. Again, these were estimated in two

ways: small dots are sizes estimated simply from the (discrete) values of the maximum significance scale  $a_{\max}$ , while crosses indicate sizes derived from two points of the profile  $y(a)$  versus  $a$ . These latter estimates are clearly more accurate than the former ones, because of the larger number of available photons. Even the poorer estimates are, however, generally within a factor of 2 of the input source size. Note that these plots are derived from simulations of fairly crowded fields, where partial overlap or interference between sources may be significant, and affect the derived properties of detections; this explains a few highly discrepant points in the scatter plots of Figures 6 and 8.

Finally, Figure 9 shows the positional agreement between input and detected sources. In the cases of multiple input counterparts for a given detection, the position is chosen as that of the counterpart having the largest number of counts. The positional agreement is better for higher significance detections and for sources in the central parts of the field of view, where the PSF is narrower. For sources detected at a (low) significance level of less than 5  $\sigma$ , in the inner 15' region of the image, the positional error radius at 90% confidence is about 30", and this reduces to 13" (slightly less than 1 pixel) for high-significance detections. For these latter detections, the 90% confidence radius beyond 45' off-axis is slightly less than 2', i.e., about equal to the local  $\sigma_{\text{PSF}}$ .

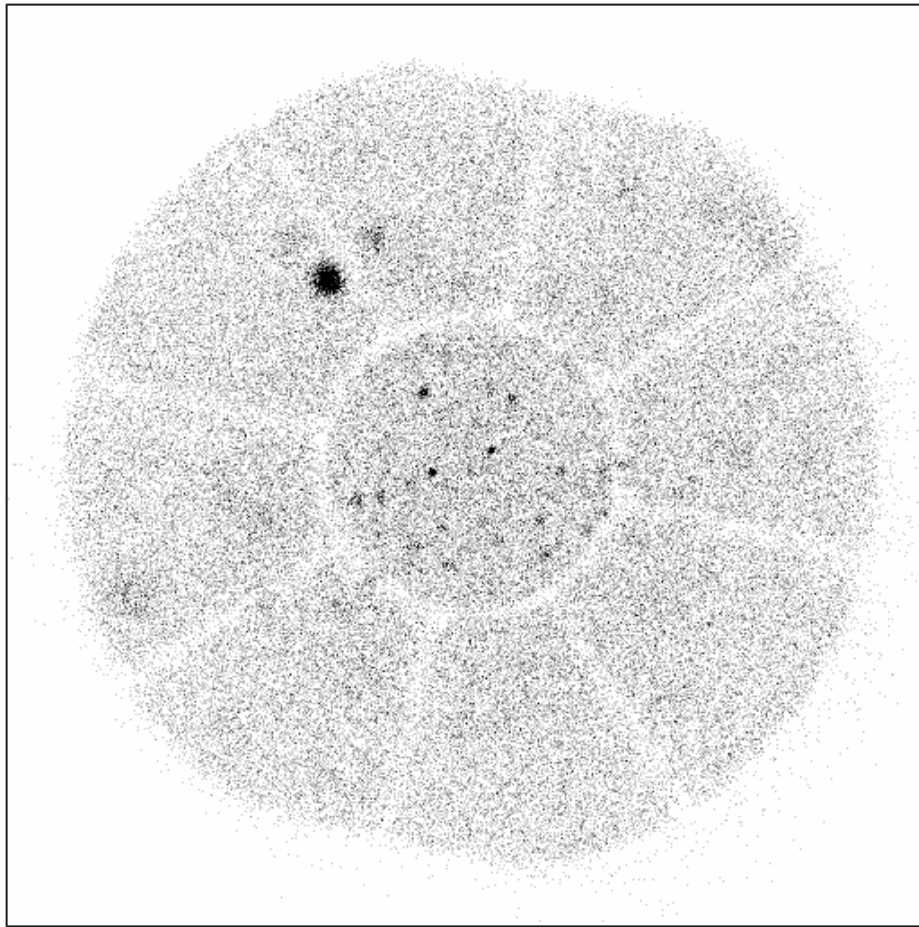


FIG. 4.—Simulated image with point sources. Simulation parameters are as in Fig. 3. In this image, 977 simulated sources are present, having a minimum of 5 photons. As is evident, most of these sources only contribute to the background and to its fluctuations.

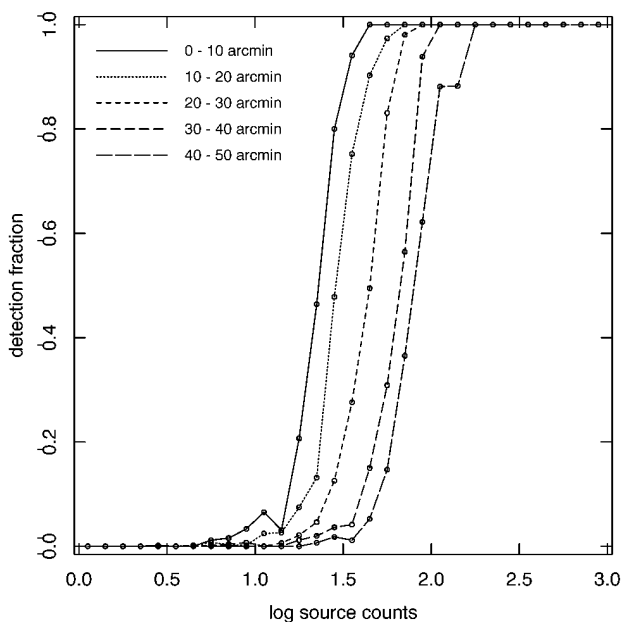


FIG. 5.—Detection efficiency evaluated on simulated data, as a function of source counts and off-axis angle. Simulation parameters are as in Fig. 3. The detection threshold is set to  $4.2\sigma$ , yielding 1.8 spurious sources per field.

On the basis of the same simulation results, we have noted that the positional error  $\delta r$  largely depends on the local PSF width  $\sigma_{\text{PSF}}$  and source significance  $k$ . For each narrow range of  $\sigma_{\text{PSF}}$  and  $k$ ,  $\delta r$  spans a range of values, whose median follows with good approximation the empirical formula  $(\delta r)_{\text{median}} = \sigma_{\text{PSF}} f(k)$ , where  $f(k) = 0.204e^{5.433/k}$ . Moreover, the quantity  $x \equiv \log_{10} [\delta r / \sigma_{\text{PSF}} f(k)]$  has a nearly Gaussian distribution, with mean  $\bar{x} = 0$  and width  $\sigma = 0.32$ . Using these formulas, it is possible to compute error radii for X-ray source identification at any desired confidence level (e.g., 90%) with good accuracy.

We have also checked the reliability of our procedure for computing upper limits, by comparing the upper limit at the positions of input sources with their input count rate. The two are consistent if the derived upper limit is always larger than the input value. Figure 10 shows that this is true in most cases; exceptions are a few upper limits below the equality line, but they do not scatter below it more than detections do (Fig. 6) and can therefore be regarded as compatible with the input count rate values as well.

### 3.3. Application to Actual PSPC Data

We have tested our algorithm on many actual PSPC archive images, chosen to present particular difficulties for an automatic analysis system. Among others, they include

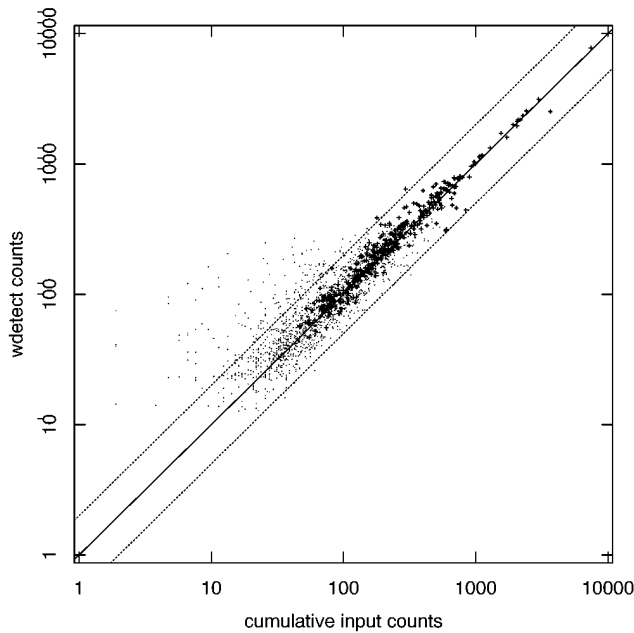


FIG. 6.—Detected vs. input counts. The solid line represents equality, and the dotted lines denote a factor of 2 difference. Small dots are zeroth-order measurements for weak sources, while crosses are more refined measurements for higher significance detections, as described in the text.

fields crowded with point sources (the Pleiades cluster, image RP200068; the Hyades cluster, RP200020), galaxies with different amounts of diffuse X-ray emission (NGC 4382, RP600008; NGC 4365, RP600009; NGC 4636, RP600016), active galactic nuclei (AGNs) (PKS 0438–436, RP700028; 1442 + 101, RP701002), and a field in the Large Magellanic Cloud (LMC) (SN 1987A, RP500100), showing a collection of all types of sources, plus strongly modulated diffuse background. The performances of existing X-ray source detection codes in these fields are often unsatisfactory, since they tend to miss sources (e.g., in crowded

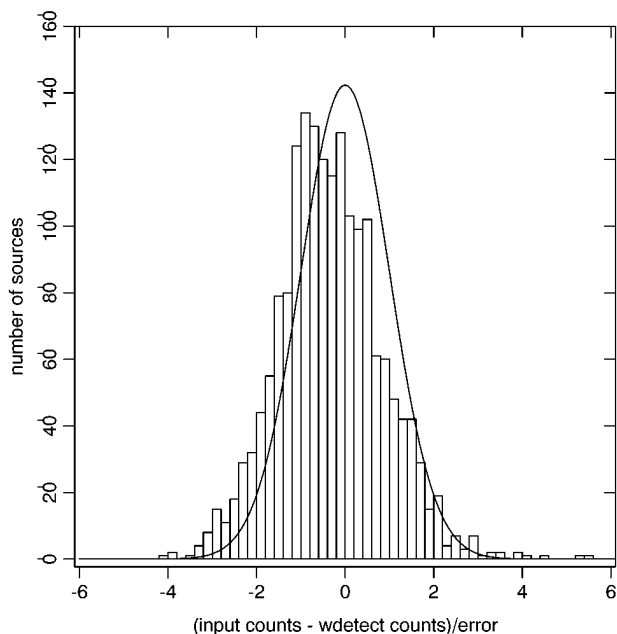


FIG. 7.—Distribution of the difference between input counts and counts estimated by the algorithm, divided by their error. Also plotted in the figure is a Gaussian with zero mean and unit variance.

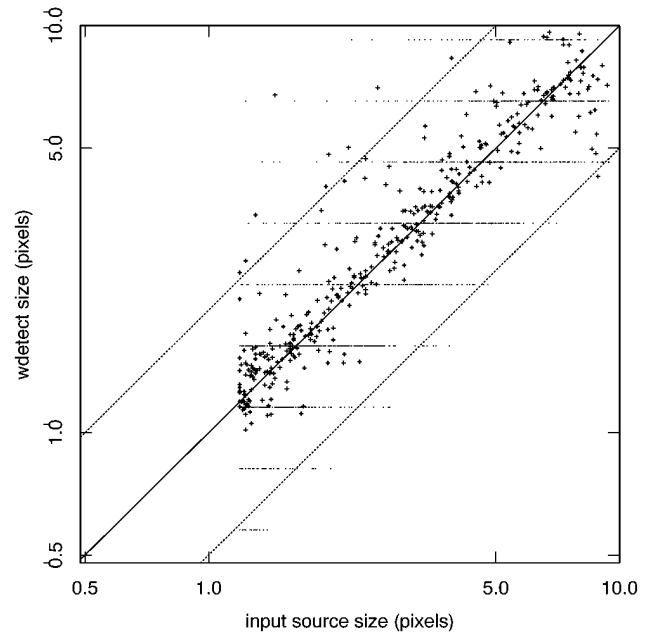


FIG. 8.—Comparison of detected and input sizes. The solid line represents equality, and the dotted lines denote a factor of 2 difference. Symbols are as in Fig. 6.

fields) or find many spurious ones (e.g., in regions containing extended sources or diffuse emission).

The analysis of the Pleiades image RP200068 offers a good opportunity to study the positional accuracy attained by our algorithm on real data, not only on simulations. Indeed, the PSF becomes increasingly different from the shape adopted in the simulations (monoenergetic and azimuthally averaged) at large off-axis angles, being significantly distorted outside the central ring of the PSPC. We have made thus a comparison between the X-ray positions given by our algorithm and the known positions of optical counterparts, with the result shown in Figure 11. Taking into account the limited statistics available (about 150 X-ray detections), the positions are as good as estimated in § 3.2 on the basis of simulated data. The median offset between X-ray and optical positions is  $-2''.2$  in right ascension, and  $1''.2$  in declination, for sources within  $30'$  of the image center. One-half of the detections with off-axis angles less than  $15'$  have offsets less than  $5''.8$ ; this number rises to  $11''.8$  for off-axis in the range  $15'–30'$  and to  $42''$  for off-axis larger than  $30'$ .

Some of the test images (smoothed with a Gaussian with  $\sigma = 1$  pixel) are shown in Figures 12a–12h, where all sources detected using our method are marked with a circle of size equal to detection scale  $a_{\max}$ . The detection threshold is set to  $4.2\sigma$ , yielding 1.8 spurious sources per field. As can be seen, the algorithm is very sensitive to any departure from a flat background, as soon as it becomes statistically significant. This is especially evident in the very complex fields of the LMC (Figs. 12c and 12d), where every small patch of diffuse X-ray emission is detected as an (extended) source. These sources are convincingly real, upon visual inspection of the images; from this point on, it is up to the user to understand what these objects are.

### 3.3.1. Comparison with Other Detection Methods

We have also compared the overall performances of our algorithm with those of algorithms that have been used to

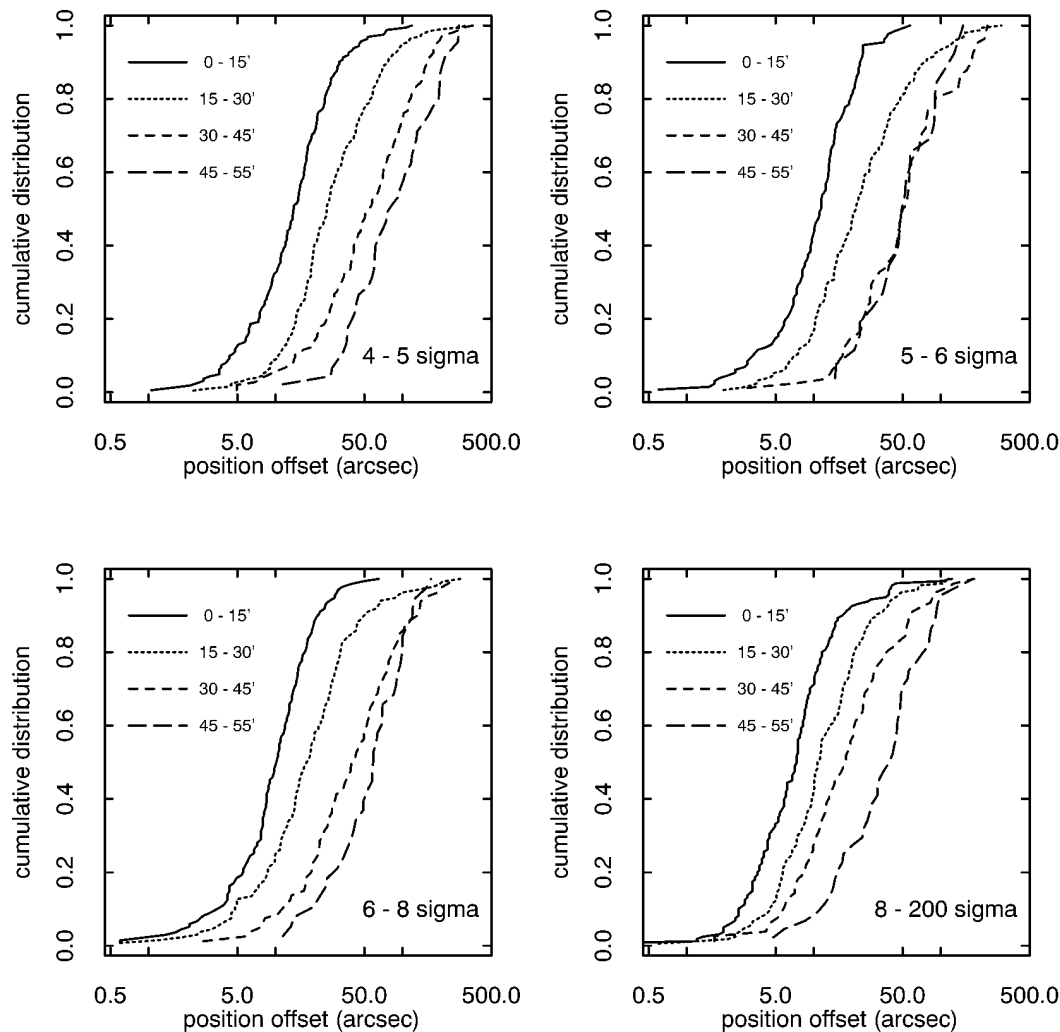


FIG. 9.—Cumulative distributions of positional errors from simulated data, as a function of detection significance and off-axis angle. Note that the cross-identification distance may be as large as a few arcminutes, even at image center in a very small fraction of cases, since it depends on the detection scale  $a_{\max}$  and not only on the PSF width  $\sigma_{\text{PSF}}$ .

produce two publicly available catalogs of *ROSAT* PSPC X-ray sources, namely, the ROSSRC (here called MPE) and WGA catalogs.<sup>3</sup> X-ray sources appearing in these two catalogs are also indicated in Figures 12a–12h, as squares (MPE) and plus signs (WGA).

Based on a careful visual inspection of these figures, a few comments are appropriate. Figure 12a is the central part of the image RP200068. There are a number of weak sources that are detected only with our method and are coincident in most cases with optical stars that are confirmed or probable cluster members, and this argues in favor of their reality as X-ray sources. There are also brighter sources, clearly real and detected with our method, which, however, are not detected by either WGA or MPE, in particular, two sources near the southern part of the inner rib (undetected by WGA), one strong source obscured by the inner rib in the northwest direction (undetected by MPE), and four sources just above the image center (undetected by MPE). Evidently, the WGA and MPE methods are inaccurate in the neighborhood of ribs and in crowded regions. Figure 12b is an enlarged view of Figure 12a, to show the ability of

our method to detect separately two pairs of very close sources, in the southeast and east directions from the image center, respectively, which are detected each as a single source by WGA and MPE.

Figures 12c and 12d are the region around SN 1987A, in the LMC (whole field of view and central part, respectively). No WGA sources are cataloged for this field, probably because of the strong diffuse emission present. Especially in the central part, it can be seen that all emission features are detected with our method, but not always by MPE (e.g., the complex bright structure northeast of the center). There are also some MPE sources not detected with the WT method, but their reality is far less clear.

Figures 12e and 12f are the galaxy NGC 4636, showing conspicuous diffuse emission around its nucleus. In this case, the spatial distributions of sources detected with the three methods are strikingly different. First, there are no WGA detections in the central part of the image (not even the bright galaxy itself), probably because of the presence of diffuse emission. On the other hand, in the same region there are many sources detected only by MPE, especially on the wings of the diffuse source NGC 4636, that may be spurious if the local background has not been accurately computed (see § 4.1 and Fig. 7 of Paper I). In the outer parts

<sup>3</sup> Available from the databases at Max-Planck Institut für Extraterrestrische Physik, and Goddard Space Flight Center, respectively.

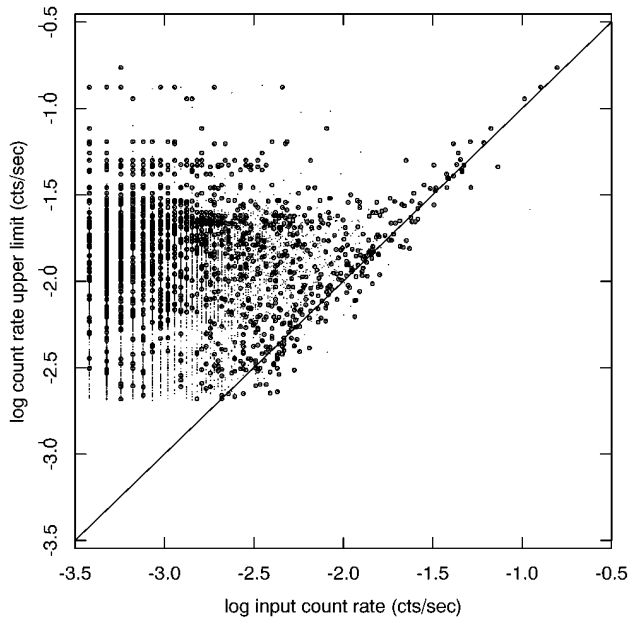


FIG. 10.—Upper limits computed for undetected sources vs. input count rates for simulated sources (*small dots*). Circles indicate input sources positionally coincident with detected sources, for which the upper limit has been set equal to the detected count rate. The derived upper limits are consistent with the input values, since most of them lie above the equality line or below it by less than a factor of 2.

of the image, instead, there are many WGA detections lacking either a MPE or WT counterpart, and most of them lie north of image center, namely, in the same direction of the large-scale background gradient in this image. We defer until the last test image a deeper study of this effect.

Finally, Figures 12*g* and 12*h* are the field of the AGN 1442 + 101. In the central part, there are a few quite obvious WT sources that are, however, missed by either WGA or MPE (or both), especially in proximity of the inner rib. We admit that there is also a fairly good MPE detection that is missed by WT, close to two stronger detected sources (westward of the center, and near the inner rib). In the outer part, again a number of WGA-only detections appear, mostly toward the northeast. To better understand the origin of these detections, we plot in Figure 13 contours of the (source-subtracted) background map of this image, with the position of sources as in Figures 12*g* and 12*h*. It can be seen that, apart from the effect of vignetting that causes the background to decrease with off-axis angle, there is a clear large-scale background gradient in the northeast-southwest direction, and most of the WGA-only detections are located along this same direction in regions of enhanced background. This fact, together with their lack of correspondence with either WT or MPE sources and their visual appearance in Figures 12*e* and 12*g*, leads us to suspect that they are spurious, arising from an improper treatment of large-scale background gradients by the WGA method.

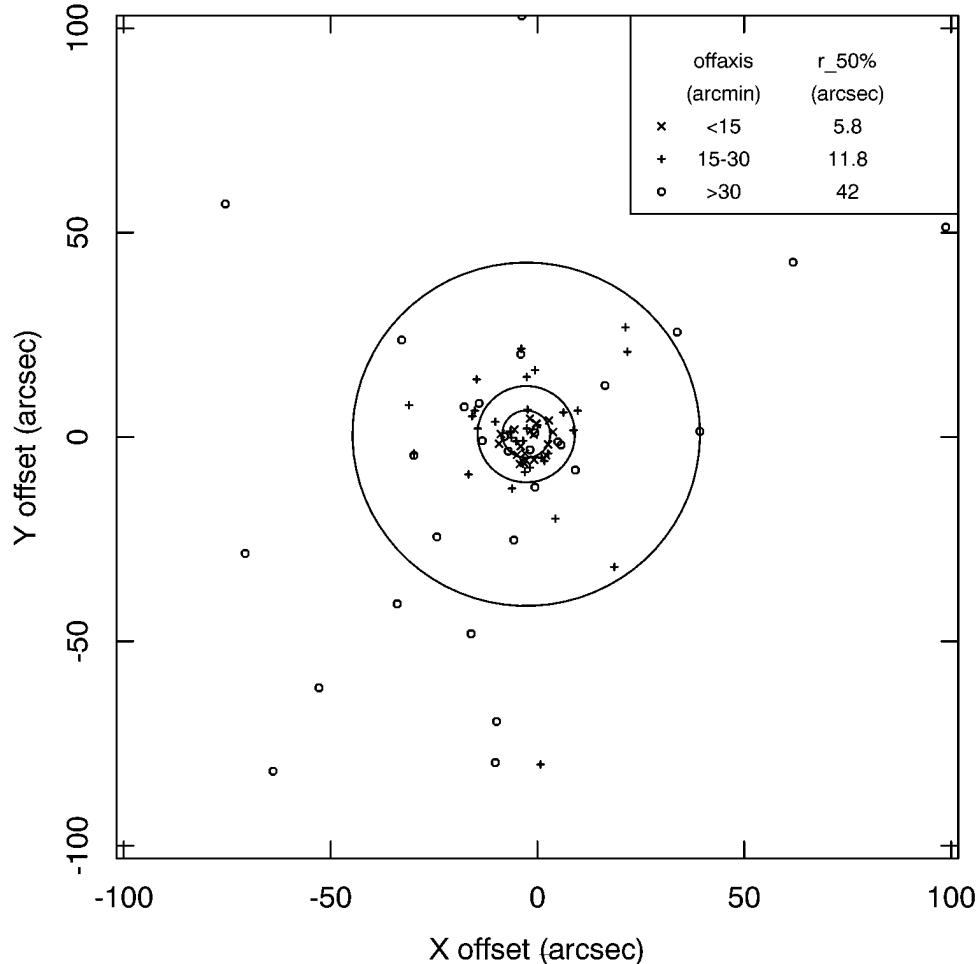


FIG. 11.—Offsets between X-ray and optical positions, for stars in the Pleiades cluster (image RP200068). Different symbols indicate different off-axis ranges: crosses indicate sources with off-axis less than 15', plus signs indicate sources between 15'–30', and small circles indicate sources beyond 30'. Large circles indicate the median offset for each off-axis range and are centered on the median offset for all sources with off-axis less than 30'.

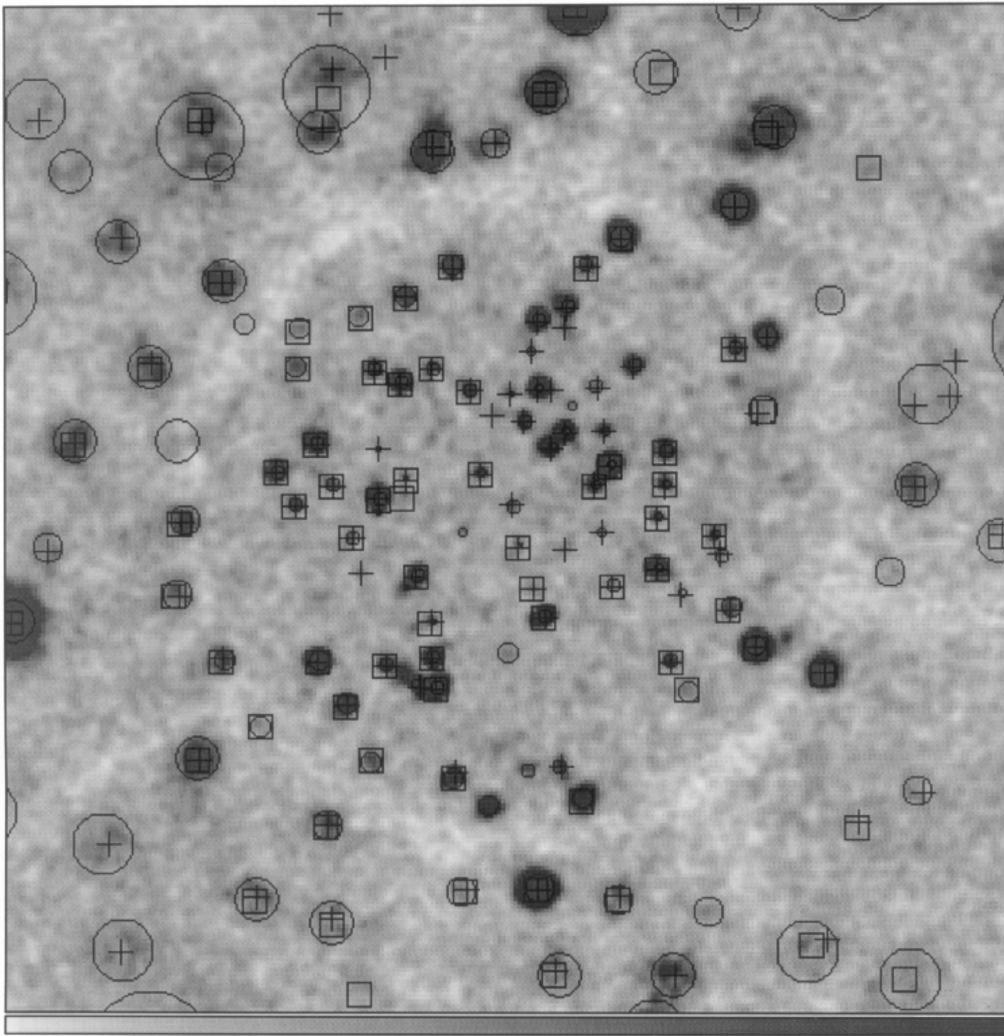


FIG. 12a

FIG. 12.—Actual PSPC images, used to compare the performances of WT, WGA, and MPE methods (north is at the top, and east is to the left). The original photon images have been smoothed with a Gaussian with  $\sigma = 1$  pixel ( $15''$ ). Circles indicate sources detected using WT with significance above  $4.2\sigma$ , and their radius is equal to the scale  $a_{\max}$  of highest significance detection [highest value of  $y(a)$ ]. Plus signs are sources from the WGA catalog, and squares are sources from the MPE catalog. See the text for details of this comparison. (a) Central part ( $32' \times 32'$ ) of Pleiades cluster (RP200068): some obvious sources are detected by WT but not by either WGA or MPE, especially close to the ribs. (b) Enlargement ( $2\times$ ) of center of Fig. 12a: two close pairs of sources are resolved by the WT, but they are detected as a single source each by the other methods. (c) Full field of view of SN 1987A, in the LMC (RP500100): no WGA sources are available for this region, while MPE misses some obvious emission features, recognized by the WT method. (d) Enlargement ( $2\times$ ) of Fig. 12c, showing more clearly the complex emission features present in the field. (e) The galaxy NGC 4636 (RP600016), full field of view, and (f) its enlargement ( $2\times$ ): many MPE detections without either a WT or WGA counterpart are spread over the diffuse envelope of this galaxy and might arise from an underestimate of the local background. In the external regions many WGA detections are found in the direction of the large-scale background gradient. (g) The AGN 1442+101 (RP701002), full field of view, and (h) its enlargement ( $2\times$ ): here again many WGA detections lie in the direction of the large-scale background gradient.

In order to perform a less subjective comparison of the performances of the three algorithms, we have chosen seven PSPC images (the same images mentioned at the beginning of § 3.3, with the exception of RP500100, i.e., SN 1987A, for which there are no entries in the WGA catalog) containing stars, galaxies, and quasars (see Table 1), and we have cross-matched sources detected with the three methods by positional agreement within  $1.5\sigma_{\text{PSF}}$ . For our algorithm, we have chosen a threshold of  $4.2\sigma$ , which yields 1.8 spurious sources per image, on average; the whole field of view was analyzed. We list in Table 1 the number of matches found, both for the full field of view and for the central region of  $25'$  radius:  $N_{\text{WT}}^{\text{tot}}$ ,  $N_{\text{WGA}}^{\text{tot}}$ ,  $N_{\text{MPE}}^{\text{tot}}$  are the number of sources detected with our wavelet algorithm (WT) and from the WGA and MPE catalogs, respectively. The next three

columns report  $N_{\text{WT}}^{\text{only}}$ ,  $N_{\text{WGA}}^{\text{only}}$ ,  $N_{\text{MPE}}^{\text{only}}$ , namely, the number of sources found *exclusively* in the WT, WGA, or MPE lists, respectively. Next, we report the number of sources common to two detection methods, namely,  $N_{\text{WT} \cap \text{MPE}}$ ,  $N_{\text{WT} \cap \text{WGA}}$ , and  $N_{\text{WGA} \cap \text{MPE}}$ . In the last column the number of detections common to all three methods is reported,  $N_{\text{all}}$ . We also describe these results, summed over all seven test images, using a diagram in Figure 14a (for the full field of view) and 14b (for the central image region). These results are not susceptible to an easy interpretation, but many interesting observations can be made anyway.

First, the number of detections common to all three methods ( $N_{\text{all}} = 197$ ) is significantly smaller than the total number of detections for each method ( $N_{\text{WT}}^{\text{tot}} = 453$ ,  $N_{\text{WGA}}^{\text{tot}} = 389$ ,  $N_{\text{MPE}}^{\text{tot}} = 286$ ). Of course, detections common

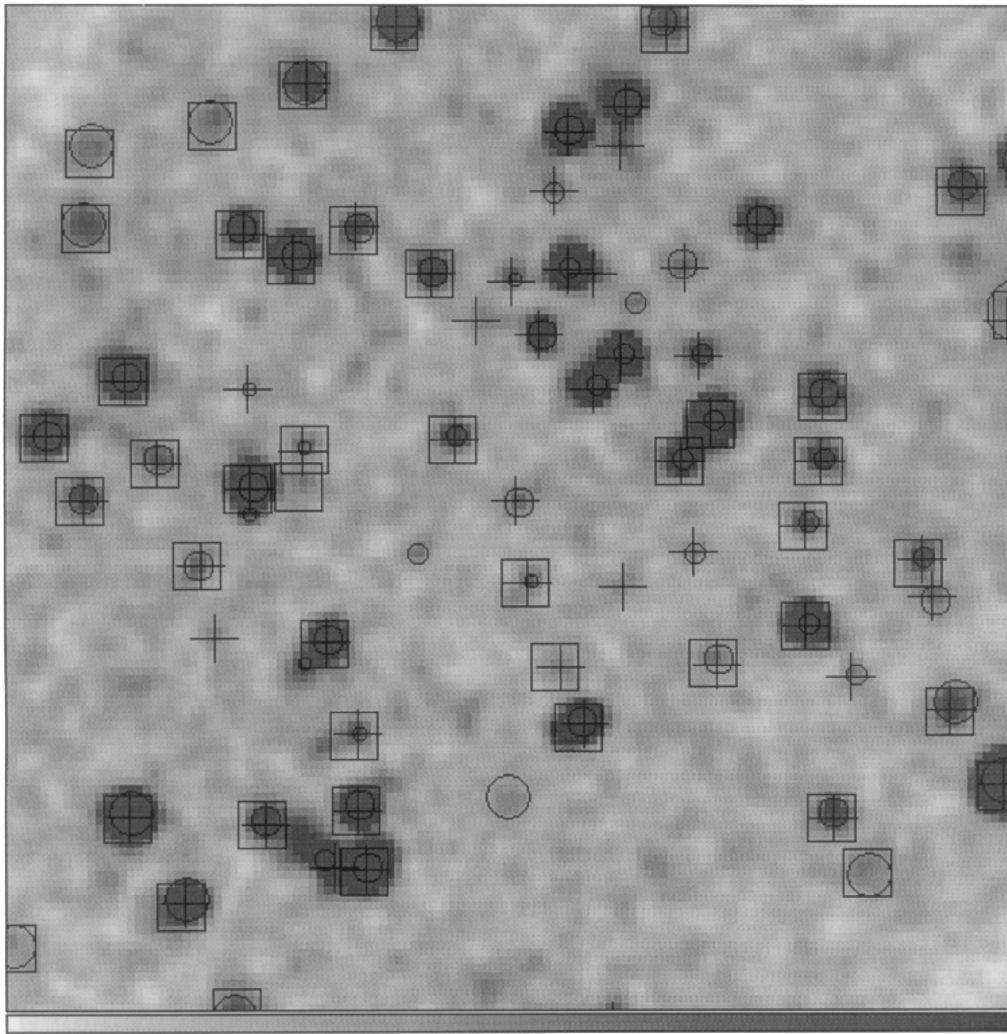


FIG. 12b

to at least two methods are most likely to be real. Each method finds many sources that are not detected by the other two: among these sources there are both spurious detections and real sources that a given method detects

more efficiently than the other two, for some reason. Among the  $N_{WT}^{only} = 134$  sources detected only with the wavelet method, we expect about 12–13 to be spurious, so that the large majority of these  $N_{WT}^{only}$  detections should be *real*

TABLE 1  
COMPARISON AMONG PERFORMANCES OF VARIOUS DETECTION ALGORITHMS

Image	$N_{WT}^{tot}$	$N_{MPE}^{tot}$	$N_{WGA}^{tot}$	$N_{WT}^{only}$	$N_{MPE}^{only}$	$N_{WGA}^{only}$	$N_{WT \cap MPE}$	$N_{WT \cap WGA}$	$N_{WGA \cap MPE}$	$N_{all}$
Full Field of View										
RP200020.....	36	34	35	7	7	9	26	25	23	22
RP200068.....	150	100	127	25	6	10	91	114	83	80
RP600008.....	36	19	27	13	3	6	16	21	14	14
RP600009.....	80	36	48	39	0	10	34	36	31	29
RP600016.....	39	41	42	11	14	29	24	10	9	6
RP700028.....	54	23	50	23	0	21	22	28	20	19
RP701002.....	58	33	60	16	2	22	31	38	27	27
Total .....	453	286	389	134	32	107	244	272	207	197
Off-Axis <25'										
RP200020.....	10	12	12	2	5	5	7	7	6	6
RP200068.....	88	58	76	11	1	5	56	70	50	49
RP600008.....	20	11	11	8	2	1	9	10	7	7
RP600009.....	39	18	20	20	1	4	17	16	14	14
RP600016.....	22	30	8	5	14	7	16	1	0	0
RP700028.....	33	15	20	16	0	5	14	14	12	11
RP701002.....	38	19	26	14	2	5	17	21	14	14
Total .....	250	163	173	76	25	32	136	139	103	101

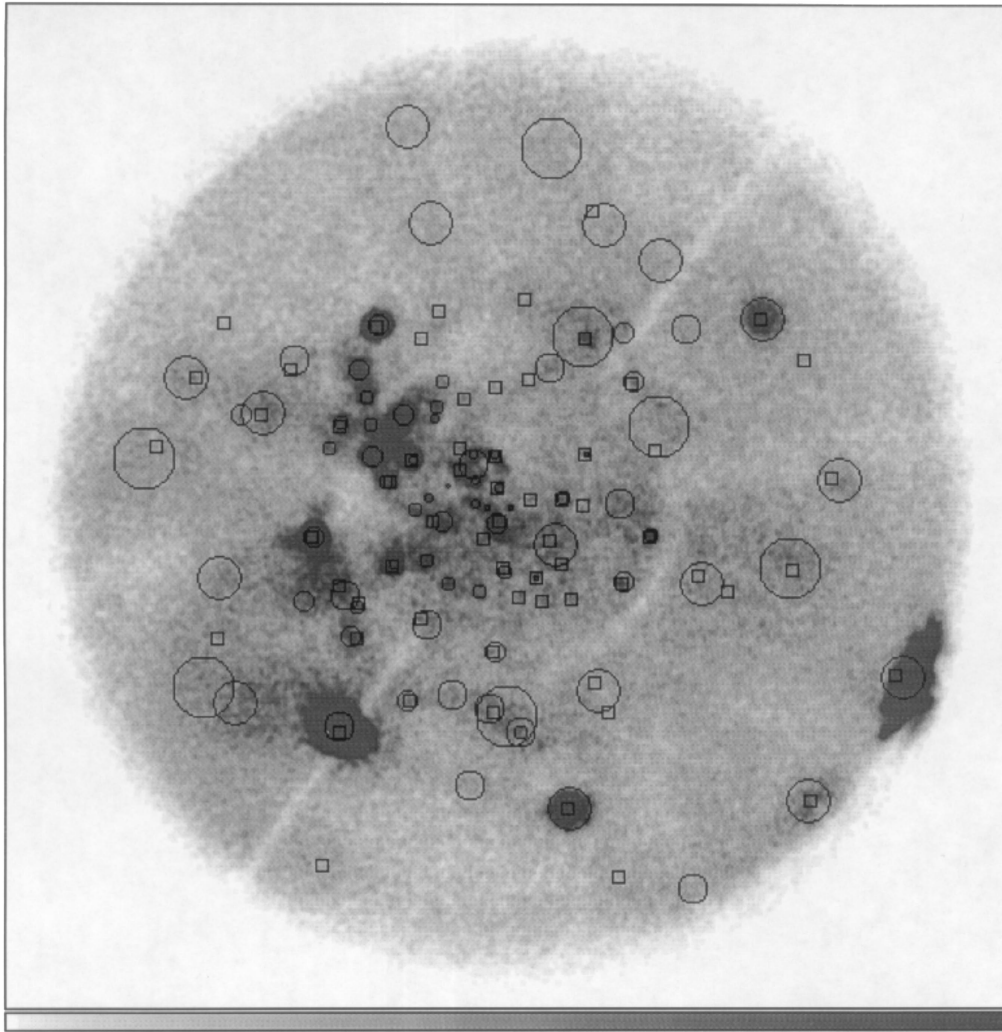


FIG. 12c

sources, missed by the other two methods. Moreover, we may get an estimate of the relative efficiency among the three methods by comparing the number of sources detected by two methods but missed by the third, namely,  $N_{\text{WT} \cap \text{MPE}} - N_{\text{all}} = 47$  (missed by WGA),  $N_{\text{WT} \cap \text{WGA}} - N_{\text{all}} = 75$  (missed by MPE),  $N_{\text{WGA} \cap \text{MPE}} - N_{\text{all}} = 10$  (missed by WT); using this relative criterion, we see that the wavelet method is the one that misses the least number of (presumably real) sources detected by the other two methods.

It remains to be seen if sources detected exclusively by WGA or MPE,  $N_{\text{WGA}}^{\text{only}} = 107$  and  $N_{\text{MPE}}^{\text{only}} = 32$ , are mostly real sources that our method is not sensitive enough to detect or consist of a large number of spurious detections. To understand this, we have evaluated the number of sources that were missed by our algorithm, on the basis of the simulations presented in the previous subsection. Namely, we have selected all input simulated sources having a number of photons larger than the nominal detection threshold at their position (assuming that we know perfectly well the local background), but which were not detected with our algorithm. It turns out that such sources are 8%–9% of the total number of detections, and are for the largest part just above the threshold. Therefore, in addition to the  $N_{\text{WT}}^{\text{tot}} = 453$  sources we detect, there may be

another approximately 40 sources not far from the detection threshold. These sources, which fall outside the “WT” circle in Figure 14a, may in principle fall in the “WGA” or “MPE” circles. In particular, the 10 sources detected by both MPE and WGA, but missed by our method, are likely a subset of these 40 missed sources, so that only 30 sources may still fall in the MPE-only or WGA-only subsamples. Therefore, the  $N_{\text{MPE}}^{\text{only}} = 32$  sources detected only by MPE are compatible with being all real, with the caveat that 14 out of 32 such sources are detected in a single image (RP600016) in a region dominated by the diffuse emission of a galaxy (see Table 1). We have presented in Paper I one such situation as a simulated test case, and we showed there that underestimating the local background in such a case leads to the detection of many spurious sources superposed to the actual extended source. For this reason we suspect that only a lower fraction (maybe one-half) of the MPE-only sources are indeed real.

On the other hand, the 107 WGA-only detections cannot be identified with those 40 sources that we may have missed; most of these may be either spurious or still real sources that for some reason fall much below our threshold but are detected efficiently using the WGA method. However, we again note that most of such WGA-only sources are detected in the outer parts of the field of view,

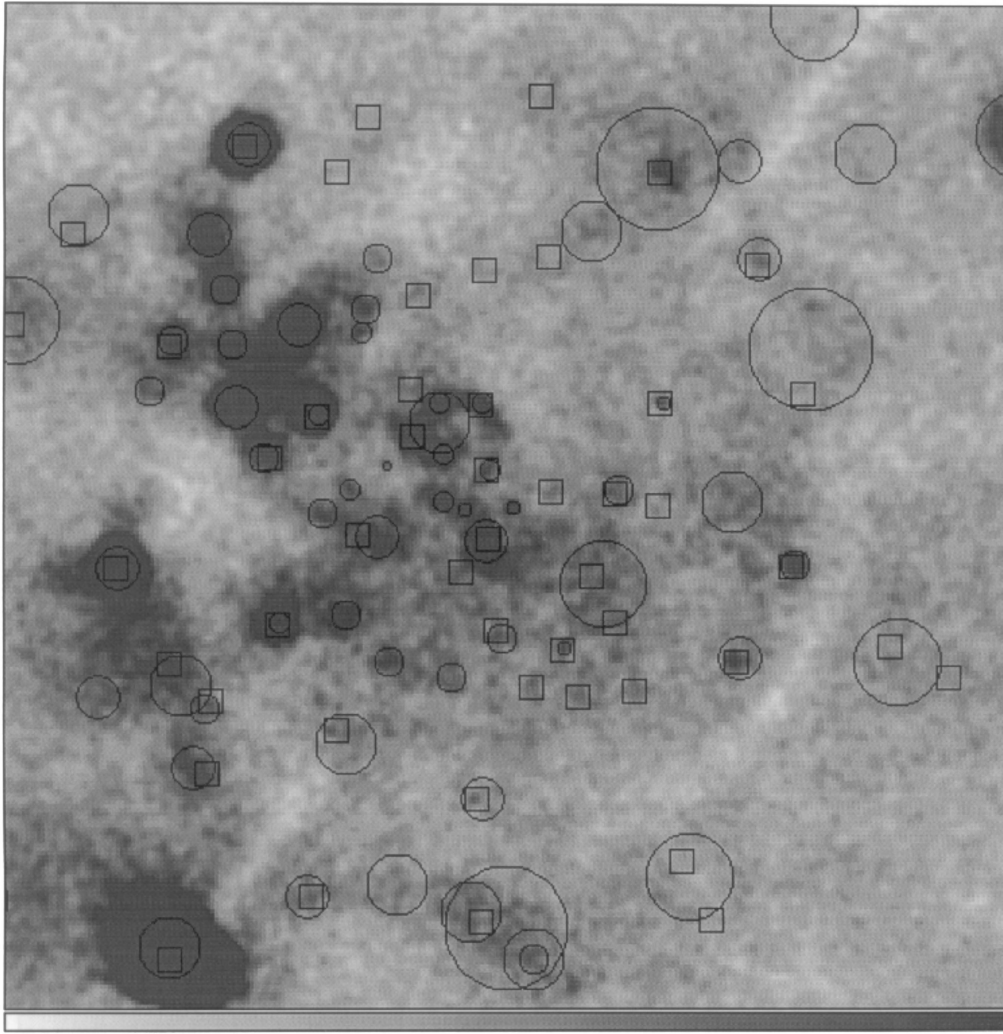


FIG. 12d

and mostly (72 sources) in three images (RP600016, RP700028, and RP701002) in which the background emission has a gradient going from one image side to the opposite. As discussed previously (see also Paper I), the adoption of a flat cosmic background model may easily yield spurious detections in these cases as well. In order to test the alternative that such WGA-only detections are real sources significantly below our threshold, we have repeated our analysis of the same images, but now using a threshold of  $3.5 \sigma$ . In this latter case, we detect a total of  $N_{\text{WT}}^{\text{tot}} = 643$  sources (instead of 453 at  $4.2 \sigma$ ), of which 300 are found only with our method (instead of 134), among which we now expect 80–90 spurious detections, because of the much lower threshold. Among the 107 WGA-only detections, undetected by the wavelets at  $4.2 \sigma$ , 14 (13%) are now detected also by our method above  $3.5 \sigma$ . Also, 8 out of 32 MPE-only detections are now common with the wavelet method. Anyhow, even using such a low threshold in our method, the number of WGA-only sources remains large ( $N_{\text{WGA}}^{\text{only}} = 93$ ), and this argues against their reality.

#### 4. DISCUSSION: THE THEORETICAL LIMIT FOR POINT-SOURCE DETECTION

It may seem surprising that our method is able to detect sources with so few total counts as  $N_{\text{src}} = 7$  at a significance

level above  $4 \sigma$ , as the results of the previous section show; such a source would not have been detected by a “local” sliding cell method, since this latter computes the significance of the source as equal to its signal-to-noise (S/N) ratio, namely,  $N_{\text{src}}/(N_{\text{src}} + N_{\text{bkg}})^{1/2} < N_{\text{src}}/(N_{\text{src}})^{1/2} = (7)^{1/2} < 3$  (where  $N_{\text{bkg}}$  is the number of background counts in the detection cell), so that the source would remain undetected even using a signal-to-noise ratio threshold of  $3 \sigma$ . However, in general, one cannot rule out the possibility of detecting sources with a very low number of photons, *provided that the background is low and very accurately known*. Regardless of a particular detection algorithm (and actual detector), if the background is known to yield  $\mu$  average expected photons (with no error on  $\mu$ ) in a “resolution element,” where we look for a source, the probability of finding  $n$  background photons in that resolution element is  $P(n) = e^{-\mu} \mu^n / n!$ . Suppose now  $\mu = 10^{-2}$  (as may occur in short PSPC exposures or using a higher resolution detector); then, e.g., for  $n = 5$  we have  $P(5) = e^{-0.01} 10^{-10} / 5! \sim 10^{-12}$ . If there are, say,  $10^4$  such resolution elements in the analyzed image, then the number of expected spurious sources with  $N_{\text{src}} = 5$  is about  $10^{-8}$  for this background value, low enough to consider nearly all such detections as reliable sources. If  $N_{\text{src}} = 2$  photons only, then  $P(2) \sim 5 \times 10^{-5}$ , which for the same number of resolution

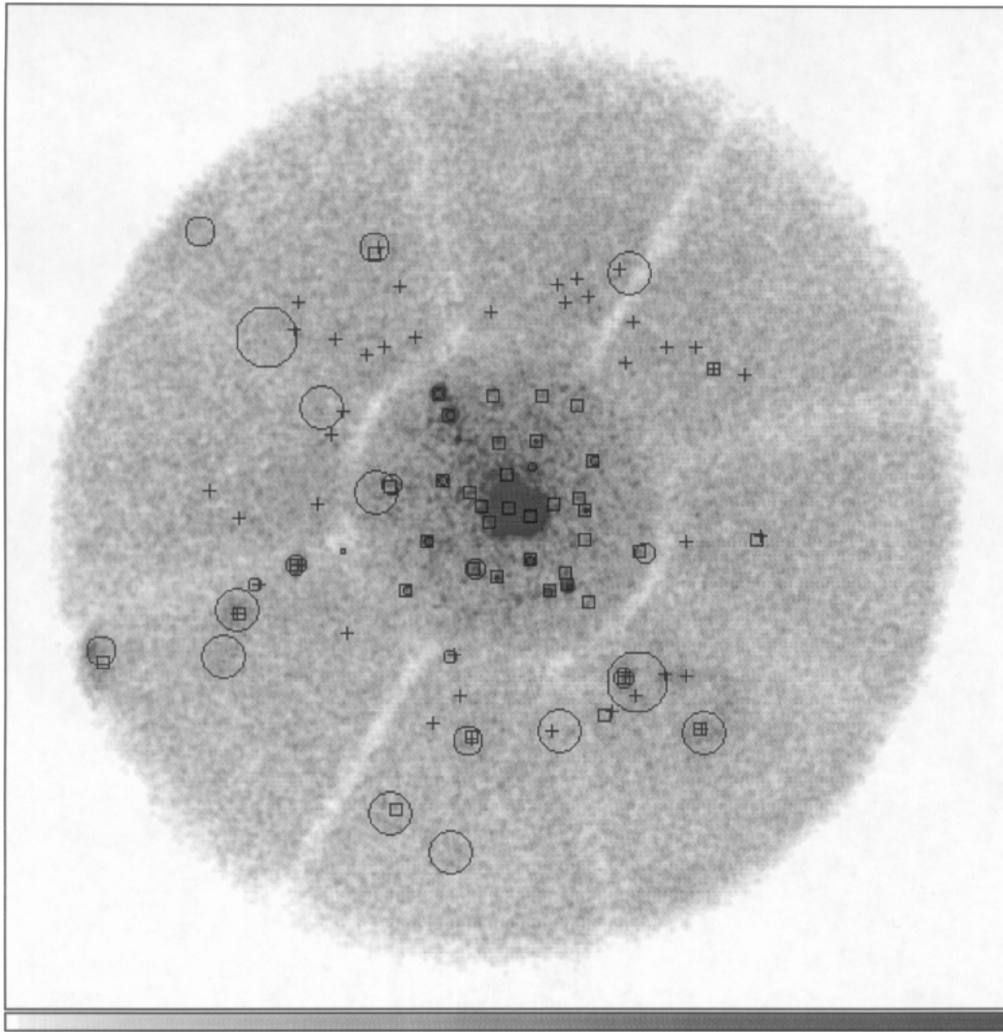


FIG. 12e

elements implies only 0.5 spurious sources per image! Is this plausible? The problem, actually, is how the background is computed: if it is determined from the same image being examined, then  $\mu = 10^{-2}$  for  $10^4$  resolution elements implies that there are only 100 background photons in the image, so that the error on the background measure is about 10%. Such an error is indeed low enough not to alter significantly the low value of the probability  $P(2)$  of finding two background photons in the same resolution element, so that, for the given background, *even sources with only two photons are real*, except for 0.5 spurious sources per image on average. The same reasoning of course does not lead to the conclusion that a single photon may yield a significant detection (if it would, our previous arguments would evidently be invalid): for one photon in a resolution element with a background  $\mu = 10^{-2}$ , we have  $P(1) = e^{-\mu}\mu = e^{-0.01}10^{-2} \sim 10^{-2}$ , which, times  $10^4$  resolution elements, yields about 100 spurious sources per image, i.e., exactly the number of photons that we know the image contains. This is consistent with all our previous reasoning. Therefore, we conclude that, in principle, there is no lower limit to the number of photons  $N_{\text{src}}$  needed by an ideal detection algorithm to detect a source, except that it must be  $N_{\text{src}} > 1$ , obtaining at the same time only a very small number of spurious sources, provided that the background density is sufficiently low and that it can be (locally)

determined with fair accuracy.

As an example, images that will be obtained with the High-Resolution Camera (HRC) of the *Advanced X-Ray Astrophysics Facility (AXAF)* will be characterized by a background rate of about  $10^{-6}$  counts  $\text{s}^{-1} \text{arcsec}^{-2}$ , according to the *AXAF Science Instrument Notebook (AXAF Science Center, 1995)*; moreover, the combined performances of the telescope and HRC detector will have a resolution element as small as  $0.5'$  for off-axis angles less than about  $4'$ . For an exposure time of  $10^4$  s, one will therefore have a background  $\mu = 2.5 \times 10^{-3}$  counts per resolution element. Proceeding as above, the probability of two background photons falling in the same resolution element is  $P(2) = 3.1 \times 10^{-6}$ , which, multiplied by the number of resolution elements in a  $4'$  circle, yields 2.25 expected spurious (two-photon) sources. With three photons, one has  $P(3) = 2.6 \times 10^{-9}$ , and only  $1.8 \times 10^{-3}$  spurious detections in the same  $4'$  radius region. Therefore, at least with an ideal method, the reliable detection of sources with only 2-3 photons is really possible in images like those obtainable with the *AXAF HRC* (or the *AXAF CCD Imaging Spectrometer [ACIS]*).

## 5. CONCLUSIONS

In this work, wavelets have proven to be an effective tool for selecting features of interest in observational data, even

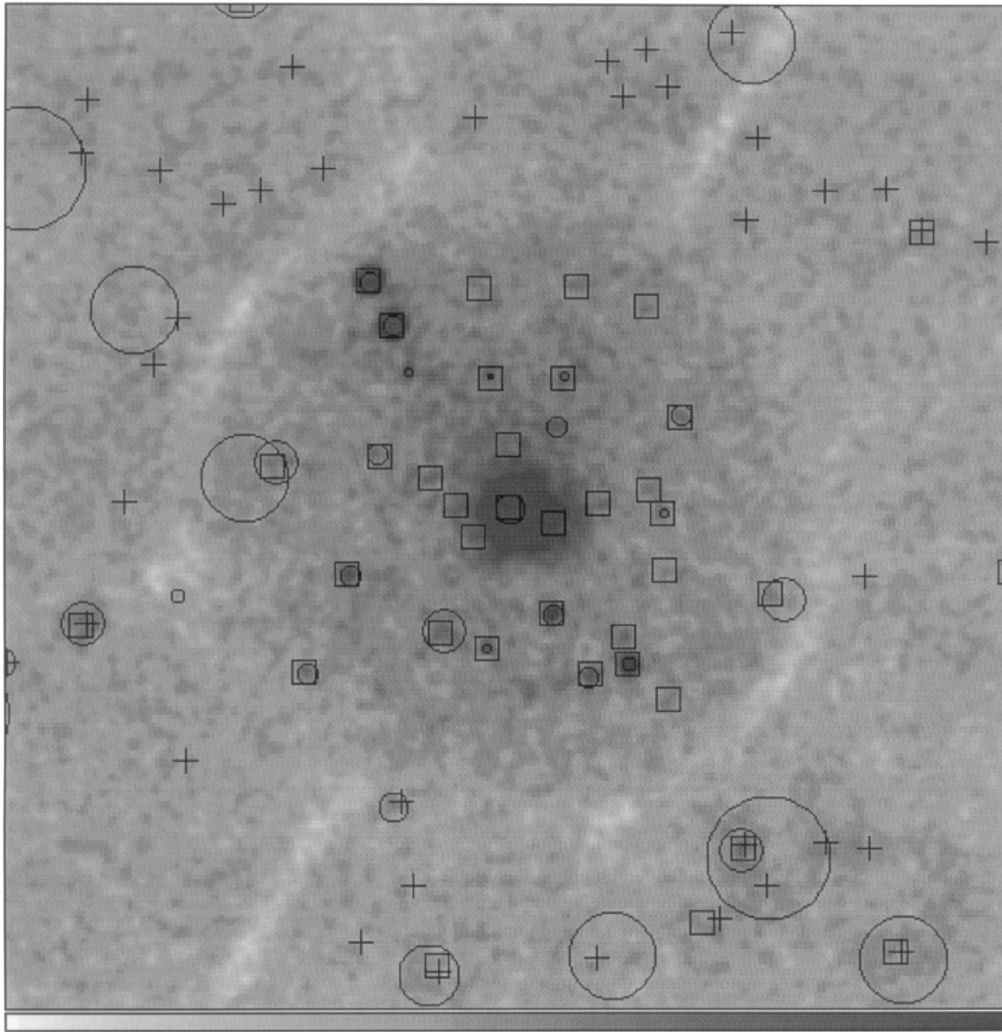


FIG. 12f

as complex as X-ray images taken with the *ROSAT* PSPC, and for discriminating them well from background noise. The ability of wavelet transforms to isolate an interesting signal from its surrounding noise was already well known, since they are successfully used for de-noising and in data compression procedures that are lossy but designed to retain most of the desired information (e.g., Press et al. 1994).

In the analysis of PSPC images, we are faced with difficulties such as image vignetting, obscuration by sharp ribs, and strong PSF variations with off-axis angle. While the general theory underlying our wavelet-based method was already presented in Paper I, here we have applied this method, optimized to analyze PSPC images. In particular, the algorithm was calibrated and tested on sets of simulated data, and its free parameters were tuned in order to maximize its efficiency to detect real sources and reject spurious ones. It was also tested on actual PSPC data, showing good performances even in complex images containing dense clusters of point sources or oddly shaped diffuse sources; in the general case, and especially in the most complex ones, our method compares favorably with the outcomes of other X-ray detection algorithms, used to generate the public domain WGA and MPE PSPC source catalogs, both in terms of sensitivity to weak sources and of reliability of

detection.

The same detection method used on PSPC data may well be applied to X-ray images obtained with the *ROSAT* HRI or other imaging detectors, with only minor changes. A few additional difficulties arise, however: first, the typical HRI background density *per resolution element* (not per square arcminute) is often lower than for the PSPC, and this makes it difficult to derive an accurate value of the local background near the field center, especially if the source density in the same region is high. The same problem will occur, to an even greater extent, in the analysis of still higher resolution images obtained with the *AXAF* HRC or ACIS detectors. Second, in the case of the *ROSAT* HRI, as preliminary tests show, it is more difficult to correct the WT for edge effects, which cause detection of spurious sources along the edge. The satellite wobbling, indeed, causes the image edge to be fuzzy, on length scales large with respect to the HRI PSF at the edge, unlike the PSPC; the length scale of such a fuzziness is, moreover, dependent on position angle along the edge, making it very difficult to apply a correction such as that applied to PSPC images. Therefore, the application of the method to this or different detectors requires that the properties peculiar to each detector be carefully taken into account. Nevertheless, the wavelet-based X-ray source detection method we have developed

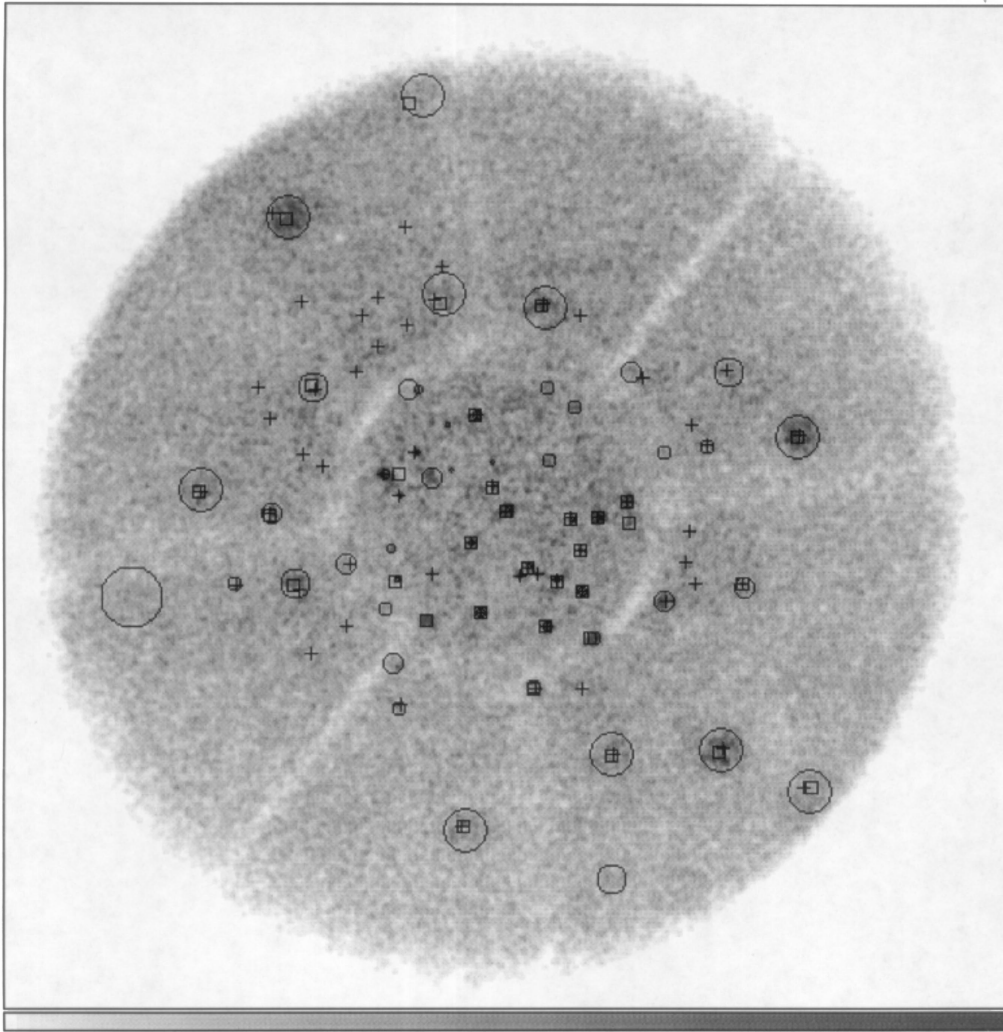


FIG. 12g

and tested here has proven to be very sensitive in the PSPC case and, once detector-specific difficulties are suitably solved, it seems promising (and we plan) to apply it to high-resolution X-ray images as well, obtained, e.g., with the *ROSAT* HRI, or with the *AXAF* HRC and ACIS in the near future.

We acknowledge support from the Italian ASI and MURST. Thanks are also due to G. Fabbiano, G. Mackie, M. Elvis, F. R. Harnden, R. Rosner, T. Maccacaro, A. Wolter, R. Della Ceca, V. Kashyap, and S. Serio for fruitful discussions and suggestions. We also thank the referee, A. Vikhlinin, for his useful comments and suggestions.

## APPENDIX A

### DERIVATION OF THE WAVELET TRANSFORM FOR A SOURCE DESCRIBED BY THE PSPC POINT-SPREAD FUNCTION

Here we derive the amplitude  $w(a)$  of the WT spatial maximum in the case of a pointlike source broadened by the PSPC PSF, taking into account its detailed shape. We adopt for it the parameterization given by Hasinger et al. (1993a), holding for the azimuthally averaged PSF profile. According to Hasinger et al. (1993a), the PSF is the superposition (sum) of various components, having a Gaussian, Lorentzian, and exponential shape, respectively.

We have already calculated in § 2 of Paper I the function  $w(a)$  for a Gaussian source (intrinsic resolution and mirror blur term); therefore, we only need here to compute  $w^{(\text{exp})}(a)$  for a decaying exponential function (focus and penetration depth term) and  $w^{(\text{scatt})}(a)$  for a Lorentzian (mirror scattering term), and to arrange all terms together to get  $w^{(\text{tot})}(a)$  for the global PSF as a function of photon energy  $E$  and source off-axis angle  $\theta$ .

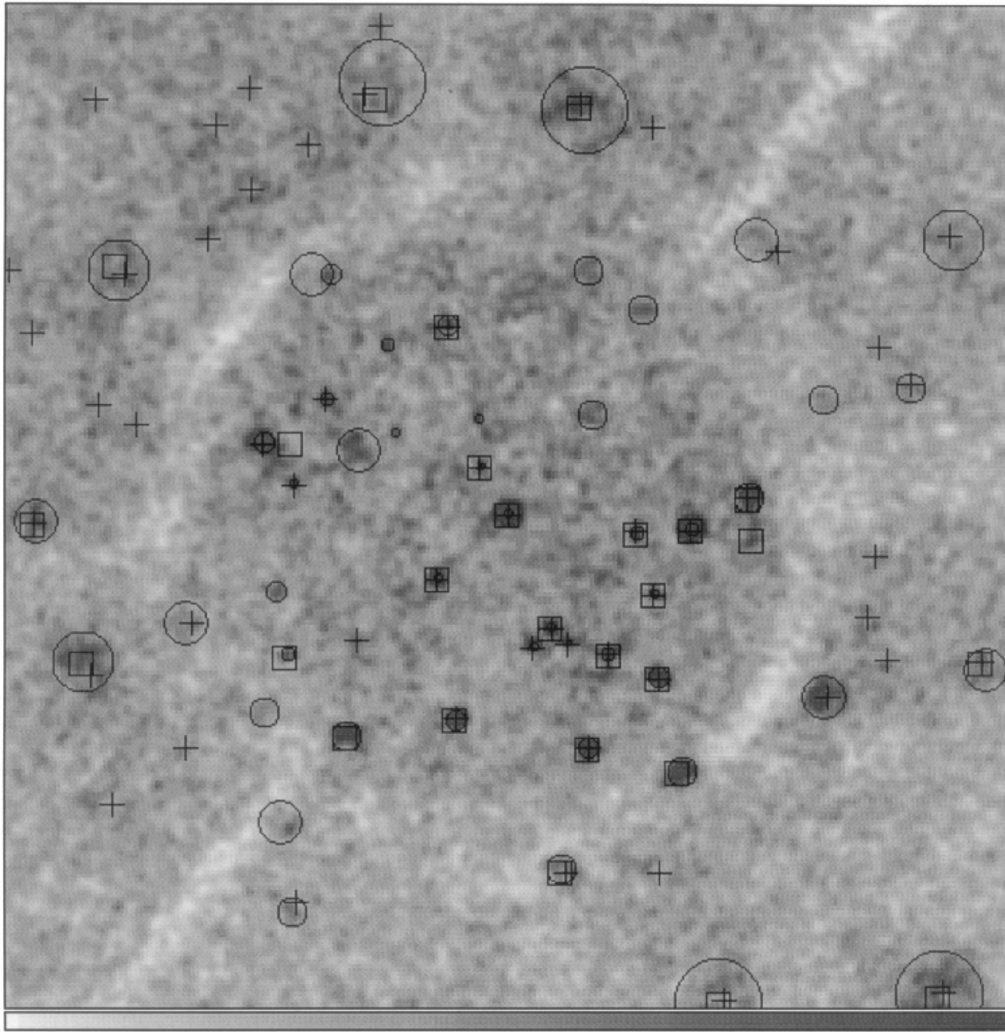


FIG. 12h

We suppose  $f(r) = e^{-r/R}/2\pi R^2$ ; then, for the exponential focus and penetration depth term the function  $w^{(\text{exp})}(a) = w(r = 0, a)$  is

$$w^{(\text{exp})}(a) = 2\pi \int_0^\infty \frac{e^{-r/R}}{2\pi R^2} e^{-r^2/2a^2} \left(2 - \frac{r^2}{a^2}\right) r \, dr = \left[ \left(\frac{a}{R}\right)^3 + \left(\frac{a}{R}\right)^5 \right] G_0\left(\frac{a}{R}\right) - \left(\frac{a}{R}\right)^4, \tag{A1}$$

where

$$G_0\left(\frac{a}{R}\right) = \int_0^\infty e^{-(xa/R) - (x^2/2)} \, dx = e^{a^2/2R^2} \int_{a/R}^\infty e^{-y^2/2} \, dy. \tag{A2}$$

The function  $G_0(a/R)$  may be expressed in terms of the error function  $\text{erf}(a/2^{1/2}R)$ . The limiting behavior of  $w^{(\text{exp})}(a)$  for  $a/R \rightarrow 0$  is easily derived, since  $G_0(0) = (\pi/2)^{1/2}$ , namely,  $w^{(\text{exp})}(a) \sim a^3$ . The limiting form of  $w^{(\text{exp})}(a)$  for  $a/R \rightarrow \infty$  is less evident from equation (A1), and we work it out in detail: first, the limiting behavior of  $G_0(a/R)$  may be found from equation (A2) (middle expression), considering that the function  $e^{-xa/R}$  in the integrand drops to zero very rapidly for large values of  $a/R$ ; in this case, we may replace the factor  $e^{-x^2/2}$  in the same integrand by the first few terms of its series expansion:

$$G_0\left(\frac{a}{R}\right) \sim \int_0^\infty e^{-xa/R} \left(1 - \frac{x^2}{2} + \frac{x^4}{8} - \frac{x^6}{48}\right) dx = \left(\frac{R}{a}\right) - \left(\frac{R}{a}\right)^3 + 3\left(\frac{R}{a}\right)^5 - 15\left(\frac{R}{a}\right)^7. \tag{A3}$$

Inserting this expression into equation (A1), we have

$$w^{(\text{exp})}(a) \sim 2 - 12\left(\frac{R}{a}\right)^2 - 15\left(\frac{R}{a}\right)^4; \tag{A4}$$

therefore,  $w^{(\text{exp})}(a) \rightarrow 2$  as  $a/R \rightarrow \infty$ , as is the case if the function  $f(r)$  is Gaussian (§ 2 of Paper I). In fact, both exponential and

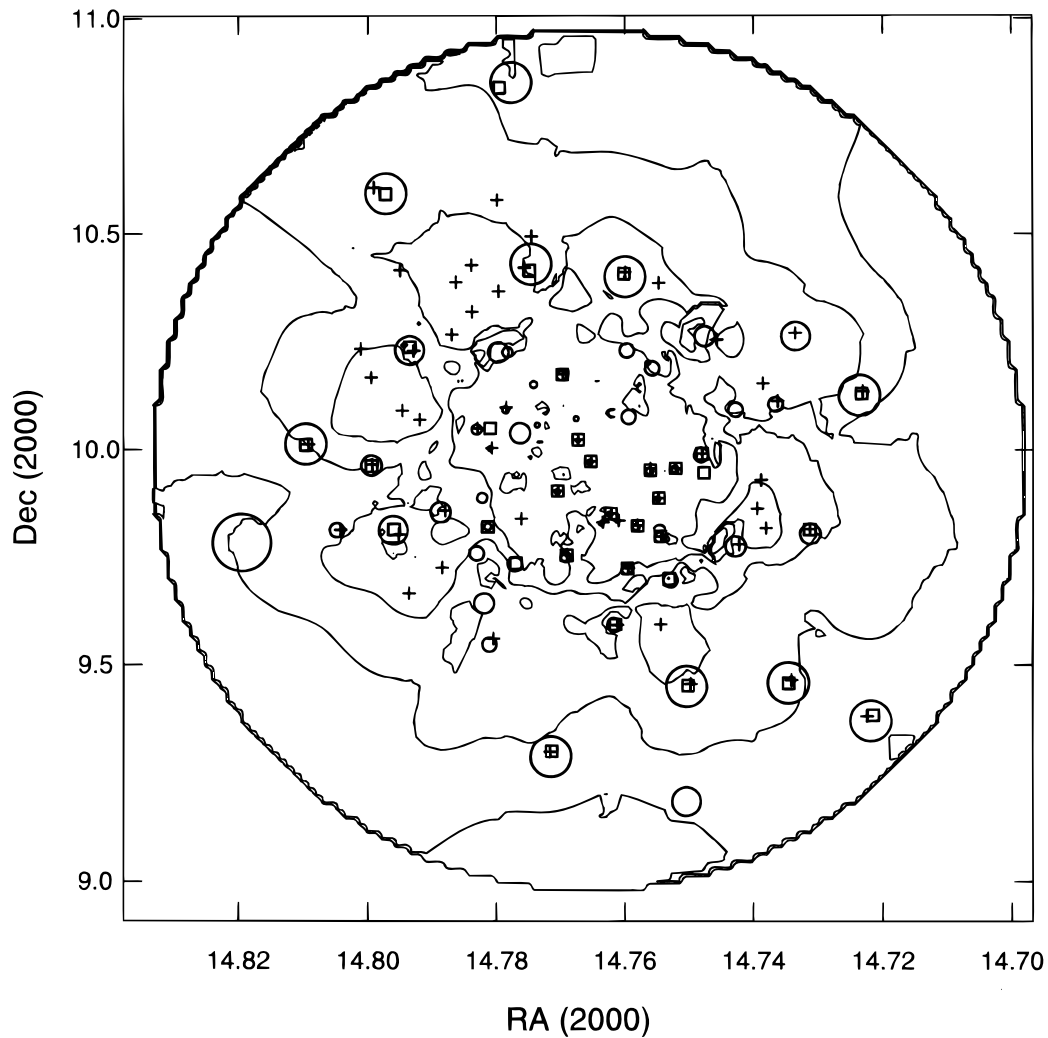


FIG. 13.—Contours of smoothed background, with detected sources removed, for the image RP701002. Sources detected by WT, WGA, and MPE methods, respectively, are indicated with the same symbols as in Fig. 12. It can be seen that (apart from the vignetting effect) the background has a gradient from the southwest toward the northeast and that many sources detected only by WGA lie precisely in regions of enhanced background emission.

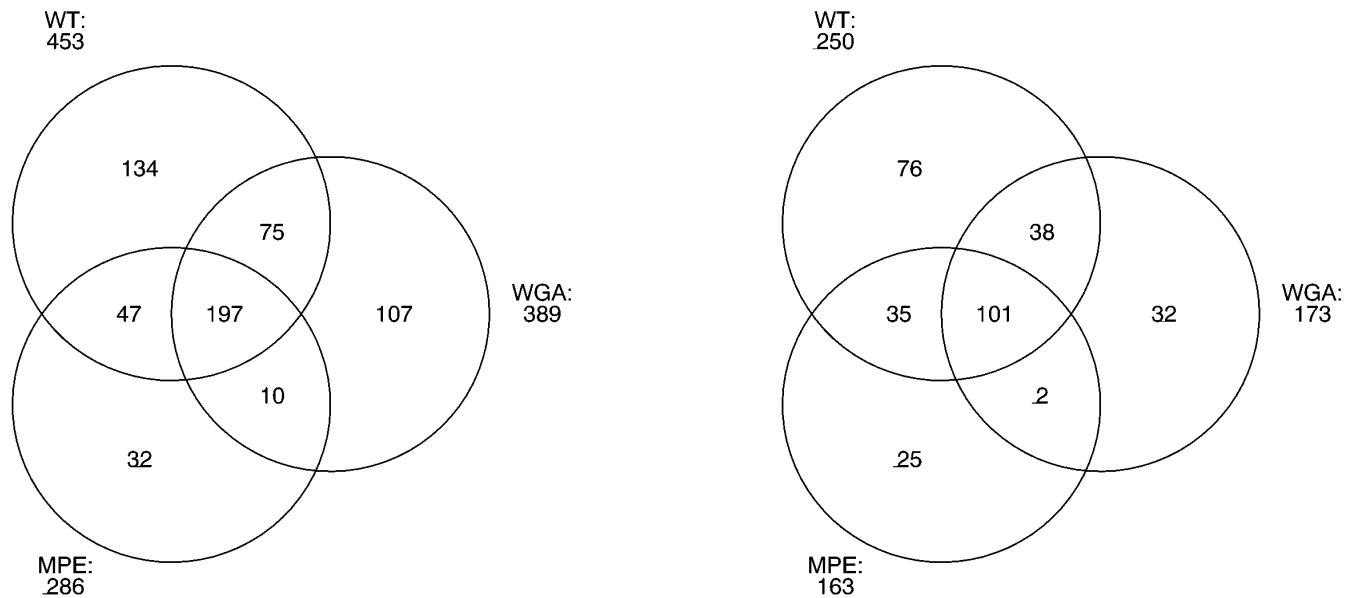


FIG. 14.—Diagram showing the number of sources detected with our method (WT), and extracted from the WGA and MPE catalogs of PSPC sources, respectively, summed on all test images of Table 1, for (a) the whole field of view and (b) the central region within 25' off-axis. Detections common to more than one method fall in the intersection between different circles.

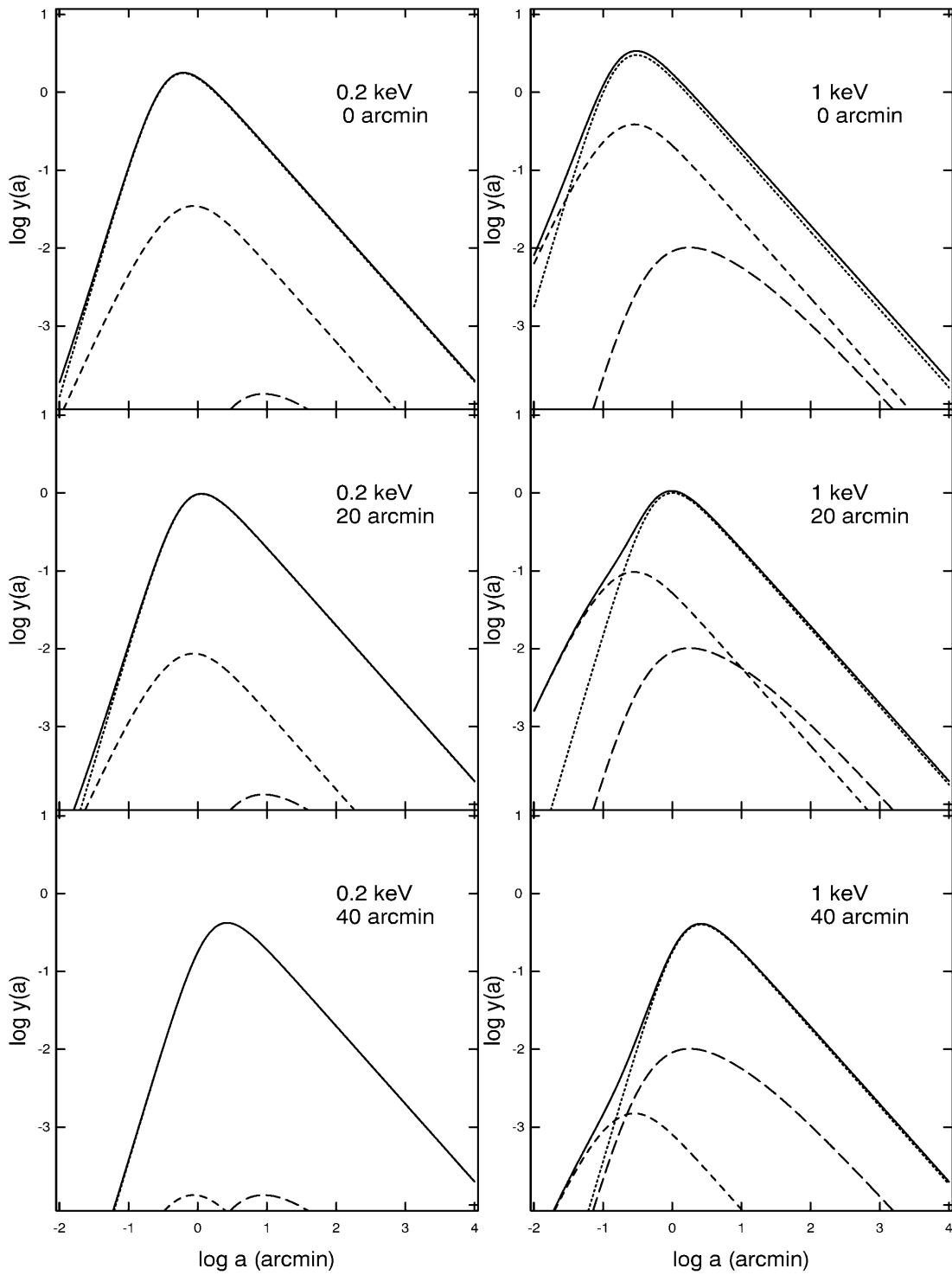


FIG. 15.—Plot of the function  $y(a)$  vs.  $a$  for the total PSF and for its components, for various energies  $E$  and off-axis angles  $\theta$ . Plotted are the total PSF (solid lines) and its components: Gaussian (dotted lines), exponential (short-dashed lines), and Lorentzian plus power law (long-dashed lines), respectively.

Gaussian functions approximate a  $\delta$ -function as  $R$  or the Gaussian  $\sigma$  tends to zero, so that  $w^{(\text{exp})}(a) \rightarrow g(0) = 2$  (§ 2 of Paper I). The function  $y^{(\text{exp})}(a) \equiv w^{(\text{exp})}(a)/a$  relative to an exponential source will behave as  $y^{(\text{exp})}(a) \sim a^2$  for  $a/R \rightarrow 0$ , and as  $y^{(\text{exp})}(a) \sim a^{-1}$  for  $a/R \rightarrow \infty$ .

The mirror scattering term is described by a Lorentzian function continued by a power law for large  $r$ :

$$f(r) = \frac{A}{1 + (r/b)^2} \quad (r \leq r_b), \quad (\text{A5})$$

$$f(r) = Br^{-\gamma} \quad (r > r_b), \quad (\text{A6})$$

where  $A$ ,  $B$ ,  $b$ ,  $\gamma$ , and  $r_b$  are given by Hasinger et al. (1993a). The WT  $w^{(\text{scatt})}(a)$  of this function is

$$\begin{aligned} w^{(\text{scatt})}(a) &= w^{\text{lor}}(a) + w^{\text{pow}}(a) \\ &= 2\pi A \int_0^{r_b} \frac{e^{-r^2/2a^2}}{1 + (r^2/b^2)} \left(2 - \frac{r^2}{a^2}\right) r dr + 2\pi B \int_{r_b}^{\infty} e^{-r^2/2a^2} \left(2 - \frac{r^2}{a^2}\right) r^{-\gamma} r dr \\ &= 2\pi b^2 A \left\{ e^{b^2/2a^2} \left(1 + \frac{b^2}{2a^2}\right) \left[ E_1\left(\frac{b^2}{2a^2}\right) - E_1\left(\frac{b^2 + r_b^2}{2a^2}\right) \right] - (1 - e^{-b^2/2a^2}) \right\} \\ &\quad + 4\pi a^2 B (\sqrt{2}a)^{-\gamma} \left[ \frac{\gamma}{2-\gamma} \Gamma\left(2 - \frac{\gamma}{2}, \frac{r_b^2}{2a^2}\right) + \frac{2}{\gamma-2} \left(\frac{r_b^2}{2a^2}\right)^{1-(\gamma/2)} e^{-r_b^2/2a^2} \right], \end{aligned} \quad (\text{A7})$$

where  $E_1(x)$  is the exponential integral, and  $\Gamma(y, x)$  is the incomplete  $\Gamma$  function. The asymptotic behavior of the function  $w^{(\text{scatt})}(a)$  may be derived from those of  $E_1(x)$  and  $\Gamma(y, x)$ , and taking into account that  $\gamma > 2$  (Hasinger et al. 1993a) and the matching relation between  $A$  and  $B$ :

$$w^{(\text{scatt})}(a \rightarrow 0) \sim -2\pi A \left[ \left(\frac{2b^2 a^2}{r_b^2}\right) + \left(\frac{b^2 e^{-r_b^2/2a^2}}{1 + b^2/r_b^2}\right) \right] \sim -4\pi A \frac{b^2}{r_b^2} a^2 [= w^{\text{lor}}(a \rightarrow 0)], \quad (\text{A8})$$

$$w^{(\text{scatt})}(a \rightarrow \infty) \sim 2\pi A b^2 \left[ \ln\left(1 + \frac{r_b^2}{b^2}\right) + \frac{2}{\gamma-2} \frac{1}{1 + (b^2/r_b^2)} \right] = 2, \quad (\text{A9})$$

where each of the two terms within brackets refers to the Lorentzian and power-law components, respectively.

The overall PSF profile is given by a linear combination of the Gaussian, exponential, and Lorentzian (plus power-law) terms, whose parameters depend on photon energy  $E$  and source off-axis  $\theta$  (Hasinger et al. 1993a). Since the WT is a linear transform, we compute the overall function  $y^{(\text{tot})}(a) \equiv w^{(\text{tot})}(a)/a$  by summing the various pieces relative to different terms. The result is plotted in Figure 15, for various values of  $E$  and  $\theta$ , including a comparison between the various terms (Gaussian, exponential, and scattering) separately. We see that the Gaussian approximation for the PSF and the corresponding  $y(a)$  profile is good for scales close to  $a_{\text{max}}$ . This implies that all computations developed in the general theory of our method (§§ 2 and 4 of Paper I), based on the assumption of a Gaussian source shape, yield valid results when the method is applied to real PSPC images, to a very good approximation.

#### REFERENCES

- Bocchino, F., Maggio, A., & Sciortino, S. 1994, *ApJ*, 437, 209  
 Damiani, F., Maggio, A., Micela, G., & Sciortino, S. 1997, *ApJ*, 483, 350 (Paper I)  
 Gursky, H., & Schwartz, D. 1974, in *X-Ray Astronomy*, ed. R. Giacconi & H. Gursky (Dordrecht: Reidel), 25  
 Hasinger, G., Boese, G., Predehl, P., Turner, T. J., Yusaf, R., George, I. M., & Rohrbach, G. 1993a, *MPE/OGIP Calibration Memo CAL/ROS/93-015*  
 Hasinger, G., Burg, R., Giacconi, R., Hartner, G., Schmidt, M., Trümper, J., & Zamorani, G. 1993b, *A&A*, 275, 1  
 Pfeffermann, E., et al. 1986, *Proc. SPIE*, 733, 519  
 Press, W. H., Teukolsky, S. A., Vetterling, W. T., & Flannery, B. P. 1994, *Numerical Recipes* (2d ed.; Cambridge: Cambridge Univ. Press)  
 Snowden, S. L., McCammon, D., Burrows, D. N., & Mendenhall, J. A. 1994, *ApJ*, 424, 714